Chapter 19

THE METHOD OF DYNAMIC IMAGING OF DIFFUSION BY EPR

Jozef K. Moscicki, Yeon-K. Shin, and Jack H. Freed

TABLE OF CONTENTS

Reprinted from: EPR Imaging and In Vivo EPR
Editors: Gareth R. Eaton, Sandra S. Eaton & Keiichi Ohno
CRC PRESS, 1991

I. INTRODUCTION

Both thermotropic and lyotropic liquid crystals appeal to scientists for their unique properties of being more or less ordered while at the same time preserving a high degree of molecular mobility. Furthermore, a number of lyotropic liquid-crystalline phases show space structures relevant to biological systems. Not surprisingly, therefore, studies of the molecular dynamics in *mesomorphic* states of condensed matter have attracted a sustained interest over the past several years.[1,2] The most fundamental characteristic of liquid-crystalline states, at least from a microscopic point of view, is the presence of long-range orientational order, while positional order is limited or absent altogether.[1] A first step towards the understanding of the relation between molecular properties and the macroscopic structure of mesophases consists of collecting information about the local behavior of the molecule subject to a mean-ordering potential. Consequently, the rotational dynamics was vigorously studied in the past. Studies were facilitated by the existence of several techniques sensitive to molecular reorientations in external fields (dielectric relaxation, FIR, Raman, nuclear magnetic resonance or NMR, electron paramagnetic resonance or EPR, and other spectroscopies). Progress in translational diffusion measurements was much slower, despite its importance for understanding the anisotropy of mass transport, critical phenomena at liquid-crystalline phase transitions,[3] and mass transport in model and biomembranes.[4] It was essentially due to the lack of reliable experimental techniques enabling such studies in liquid-crystalline materials.

One can divide experiments designed to measure the translational diffusion constant, D, into two general categories. A "macroscopic" method involves diffusion over distances, several orders of magnitude larger than molecular dimensions, whereas a "microscopic" method measures diffusion over dimensions on the order of molecular lengths. Early efforts on mesomorphic materials were essentially restricted to the first category and involved impurity diffusion across the sample. These include chemical,[5] optical,[6,7] and radioactive[8,9] probes, charge carriers,[10] and NMR with pulsed gradients.[11] In the last decade, there was a rapid development in experimental techniques which permit the diffusion coefficient to be measured spectroscopically. Macroscopic diffusion coefficients are directly measured from NMR field-gradient spin echoes.[12-15] Macroscopic techniques employed to measure diffusion of spin probes and spin labels include that of Sheats and McConnell[16-18] which requires selective photobleaching of a sample and that of Ahn[19] which applies the capillary-diffusion method[20] to EPR and requires a great deal of measurement time. Recently, EPR imaging has been intensively applied to study mass transport in liquids, thermotropic liquid crystals, model membranes, and biologically relevant polymers.[21-37]

Typical examples of microscopic methods used in the translational dynamics studies are the measurement of Heisenberg spin exchange (HSE) between colliding radical pairs,[38,39] the temperature and frequency dependence of T_1, T_{1D}, and $T_1\rho$ in NMR,[40] and of quasielastic neutron scattering (QENS).[41]

Of course, one should employ a combination of microscopic and macroscopic measurements to better understand the details of molecular motions important for diffusion on all scales of distance. Moreover, both the magnitude and the anisotropy of macroscopically measured diffusion coefficents are important both for discriminating between microscopic models of diffusion in liquid crystals and in models of molecular dynamics near the liquid-crystalline phase transitions.

Despite the evident applicability of NMR or HSE-EPR and QENS techniques in studying the translational diffusion on macroscopic or microscopic scales, the diffusion data have a significant amount of uncertainty, and there is a need for other methods for an independent and reliable verification. For example, in the pulsed-field gradient NMR methods, the diffusion coefficient is determined from the ratio of the spin-echo amplitude with and without the gradient pulse, all other parameters being kept constant. Since the gradient enters into

the result quadratically,[11-14] the absolute accuracy of the diffusion coefficient is mainly limited by the accuracy with which the magnetic-field gradient can be determined. Next, the use of NMR relaxation times, HSE-EPR, or QENS techniques gives results which depend heavily on the particular theoretical models of the molecular dynamics that are utilized in order to extract D, and systematic errors are difficult to estimate. Additionally, HSE-EPR and NMR give an average diffusion constant only; therefore, these methods are useless in anisotropy studies. Thus, there is a constant need for new techniques to study the translational diffusion, and the use of EPR imaging for this purpose is one of the latest efforts.

There are, indeed, special reasons to have developed EPR-imaging methods. First, there is HSE-EPR for studying translational diffusion over microscopic dimensions. Second, EPR is routinely used to obtain information about the rotational dynamics of spin probes.[42,43] A convenient technique for measuring macroscopic translational diffusion coefficients for spin probes, especially in anisotropic media, would enable simultaneous, yet independent, studies of rotational and translational motions on the same sample. Such studies have been carried out in the authors' laboratory.[33,34,37]

The use of EPR imaging for "dynamic samples" to investigate transport phenomena has been accomplished in just a few laboratories.[21,23,24,26,30-37] The term "dynamic sample" is used to describe a sample in which, with the passage of time, this inhomogeneous distribution will tend toward a homogeneous distribution via translational diffusion. The first experiments to measure diffusion coefficients required either long experimental times[21,24,30,31] (several days) or assumed an idealized distribution of the spin-probe concentration profile.[23] Quite recently, a significant breakthrough in the development of the technique of dynamic imaging of diffusion (DID) by EPR (DID-EPR) was made by applying Fourier-space analysis of the data,[32] and, subsequently, the methodology of the experiment and the numerical analysis of the data was improved.[35-37] Thus, at present, it is possible to measure, within an hour, by DID-EPR diffusion coefficients of the order of 10^{-7}cm^{2}s^{-1} with an accuracy better than a few percent, and of the order of 10^{-9}cm^{2}s^{-1} with an accuracy of 10 to 20%. This relatively short experimental time permits one to perform a multiple-diffusion measurement on the same sample, e.g., to perform a series of measurements at different temperatures.[33,34,37]

In the following sections of this chapter, an in-depth review of the authors' method is given. The basic theoretical fundamentals are outlined, and experimental details and the accuracy and precision of DID-EPR are considered. The final sections discuss translational-diffusion results obtained to date and perspectives for further developments in the DID-EPR technique.

II. BASIC THEORETICAL CONCEPTS

The time evolution of the concentration profile results from the translational diffusion of spin probes, as a sample with an inhomogeneous (initial) distribution of spin probes tends to a state of homogeneous (final) distribution. A diffusion coefficient can then be determined from changes of the distribution of spin probes in time. The spin probes can be used as markers for the imaging of diffusion only if the EPR signal is independent of the concentration. It is, therefore, very important that, at any time during the experiment, the concentration of spin probes at any point in a sample is low enough that the line-broadening from Heisenberg spin-exchange (HSE) can be neglected. The analysis of the concentration profiles is facilitated if the concentration of spin probes is also low enough for the translational diffusion to obey Fick's Second Law:[44]

$$\frac{\partial C(x,t)}{\partial t} = D_x \frac{\partial^2 C(x,t)}{\partial x^2} \tag{1}$$

where D_x is the diffusion constant.

The simplest and most ideal diffusion experiment would be the diffusion of spin probes from an instantaneous point-source (δ-function). If the source is placed at $x = 0$ at $t = 0$, then the solution to Equation 1 is:

$$C(x,t) = \frac{C_o}{\sqrt{4\pi D_x t}} \exp\left\{-\left(\frac{x}{\sqrt{4D_x t}}\right)^2\right\}$$

$$= \frac{C_o}{\sqrt{2\pi \cdot \sigma_x^2(t)}} \exp\left(-\frac{x^2}{2 \cdot \sigma_x^2(t)}\right) \tag{2}$$

For example, the concentration profile is a Gaussian curve for all time, $t > 0$, although the variance of the profile, $\sigma_x^2(t) = 2D_x t$, is constantly changing.

For an arbitrary initial distribution of spin probes, the solution, in the absence of any boundary effects, can be written as a convolution of the initial distribution $C(x,t = 0)$ with the Green's function, $G(x,t)$:[44]

$$C(x,t) = \int_{-\infty}^{\infty} C(x',t = 0)G(x - x',t)dx'$$

$$= \frac{1}{\sqrt{4\pi D_x t}} \int_{-\infty}^{\infty} C(x',t = 0)e^{-(x-x')^2/4D_x t}dx' \tag{3}$$

Equation 3 may be adapted easily to specific boundaries, such as reflecting walls at $x = 0$ and L.[45]

Although determination of the diffusion coefficient for a point source is straightforward (see Equation 2), an arbitrary initial distribution makes the task more difficult and less accurate. To facilitate the analysis, therefore, it is advisable to work with simple and well-defined initial concentration profiles. The preparation of a point source of spin probes is not feasible experimentally, and the initial distribution always extends over a finite distance in practice. The simplest model of an extended-source is a square-function of width $2x_o$ centered at $x = 0$:

$$C(x,0) \begin{cases} = 0 & \text{if } |x| > x_o \\ = C_o & \text{if } |x| \leq x_o \end{cases} \tag{4}$$

Then, from Equation 3 the concentration profile at a later time t is given by[44]

$$C(x,t) = \frac{1}{2}C_o\left\{\text{erf}\left(\frac{x_o - x}{\sqrt{4D_x t}}\right) + \text{erf}\left(\frac{x_o + x}{\sqrt{4D_x t}}\right)\right\} \tag{5}$$

where erf(x) denotes error function. With passing time, Equation 5 more closely resembles a Gaussian curve and for $D_x t > x_o^2$ it may be written to a good approximation as:

$$C(x,t) \cong \frac{C_o}{\sqrt{2\pi\sigma_x^2}} \exp\left\{-\frac{1}{2}\frac{x^2}{\sigma_x^2}\right\} \tag{6}$$

Therefore, with time, the concentration profile becomes similar to the case of diffusion from

a point source. Furthermore, the narrower the initial distribution, the shorter the time after which the concentration profile can be considered Gaussian; this was found to be true for most of the experimentally prepared narrow initial distributions.[31,32,34,35] Since the variance in Equation 6 might be thought of as having evolved in time from the variance of some hypothetical Gaussian initial distribution, δ_x^2, we can write

$$\sigma_x^2 = \delta_x^2 + 2D_x t \tag{7}$$

Although δ_x cannot be identified with x_o, both quantities are of the same order, as can be demonstrated from a "best fit" of the form of Equation 6 to Equation 5 for $D_x t > x_o^2$. It is, therefore, conceptually justified to consider concentration profiles that are well-developed in time as Gaussian curves. (In the following discussion, the term "Gaussian" is used in this sense.)

The easiest way of analyzing a Gaussian concentration profile is to use a semilogarithmic scale. For example, the logarithm of Equation 2 gives:

$$\begin{aligned} \ln[C(x,t)] &= -(4D_x t)^{-1} \cdot x^2 + \ln[C_o/\sqrt{4\pi D_x t}] \\ &= -(2\sigma_x^2(t))^{-1} \cdot x^2 + \ln[C_o/\sqrt{2\pi\sigma^2(t)}] \end{aligned} \tag{8}$$

On the basis of Equation 8 one can easily calculate $\sigma_x^2(t)$ for a given t. Since, in practice, the time of initialization of diffusion is ill-defined, one must repeat the experiment at least at a second t in order to determine D_x.

Analysis of the concentration profile in x-space (the space-domain analysis) depends heavily on the assumption that the profile has developed from an initial point source, i.e., it is Gaussian.[31] This arbitrary assumption can be avoided if one analyzes data in the Fourier domain. Following the convolution theorem,[46] the Fourier transform (FT) of both sides of Equation 3 yields:

$$C(k,t) = G(k,t) \cdot C(k,t = 0) \tag{9}$$

$$\begin{aligned} \ln C(k,t) &= \ln G(k,t) + \ln C(k,t = 0) \\ &= -4\pi^2 D_\xi t \cdot k^2 + \ln C(k,t = 0) \\ &= -2\pi^2 \sigma_\xi^2(t) \cdot k^2 + \ln C(k,t = 0) \end{aligned} \tag{10}$$

where k is the inverse wavelength and $C(x,t) \overset{FT}{\longleftrightarrow} C(k,t)$ and $G(x,t) \overset{FT}{\longleftrightarrow} 6(k,t)$ are "Fourier transform pairs". Recall that, in general, all functions in Fourier-space are complex.

One can then make use of Equation 10 to determine D_x in the Fourier-domain analogous to Equation 8 in the space-domain analysis, for an arbitrary initial concentration profile.

How then does the DID-EPR experiment monitor the evolution of the concentration profile in time? The simplicity of the DID-EPR experiment is in the fact that we are monitoring solely the component of diffusion in the direction of the one-dimensional (1-D) magnetic-field gradient, even though the sample is three-dimensional (3-D). Consider a 1-D inhomogeneous concentration of spin probes along some arbitrary direction x at time t, C(x,t); Also assume that a uniform magnetic-field gradient parallel to x can be generated, i.e., $B' = \nabla_x B$. In the presence of the gradient, x becomes linearly mapped onto B and vice versa; one may then consider both variables equivalent. For the convenience of further discussion, a universal variable $\xi = x \cdot B' = (B - B_o)$ is introduced in place of x and B, where B_o is a constant and ξ is in the same units as B. It is easy to verify by substitution

that the basic equations of diffusion (i.e., Equations 1 through 10) hold also as a function of ξ, with D_x, σ_x^2, and δ_x^2 replaced by $D_\xi = D_x \cdot B'^2$, $\sigma_\xi^2 = \sigma_x^2 \cdot B'^2$, and $\delta_\xi^2 = \delta_x^2 \cdot B'^2$, respectively. (For consistency, note that ξ is the same variable as ξ_B introduced before.[6])

The absorption-EPR spectrum in the presence of the magnetic-field gradient, $I_g(\xi,t)$, is a superposition of the signals of spin probes at different positions; i.e., $I_g(\xi,t)$ is the convolution of the absorption spectrum in the absence of magnetic-field gradient, $I_o(\xi)$, with the normalized concentration profile:[31,35]

$$I_g(\xi,t) = \int_{-\infty}^{\infty} C(\xi',t) I_o(\xi - \xi') d\xi' / \int_{-\infty}^{\infty} C(\xi') d\xi' \qquad (11)$$

Henceforth, the normalization factor $\int_{-\infty}^{\infty} C(\xi')d\xi'$ will be omitted, assuming that $C(\xi)$ is always the normalized concentration profile. To extract the concentration profile, again take advantage of the convolution theorem.[46] The FT of both sides of Equation 11 gives:

$$I_g(\kappa,t) = C(\kappa,t) I_o(\kappa) \qquad (12)$$

where $I_g(\xi,t) \overset{FT}{\longleftrightarrow} I_g(\kappa,t)$, $I_o(\xi) \overset{FT}{\longleftrightarrow} I_o(\kappa)$, and $C(\xi,t) \overset{FT}{\longleftrightarrow} C(\kappa,t)$ are "Fourier-transform pairs", and κ is the inverse wavelength associated with ξ. Dividing both sides of Equation 12 by $I_o(\kappa)$, we obtain $C(\kappa,t)$, which can be analyzed in terms of Equation 10 (Fourier-domain), or by performing the inverse FT of $C(\kappa,t)$:

$$C(\xi,t) = \int_{-\infty}^{\infty} e^{2\pi i \kappa \xi} C(\kappa,t) d\kappa = \int_{-\infty}^{\infty} e^{2\pi i \kappa \xi} \frac{I_g(\kappa,t)}{I_o(\kappa)} d\kappa \qquad (13)$$

one may analyze $C(\xi)$ with the aid of Equation 8 (space-domain). Note, that, in principle, data analysis in the Fourier-domain should not only be simpler, but also produce significantly smaller error in D_ξ, as a result of significantly less data manipulation, i.e., there is no need for the inverse FT (see Equation 13). However, the Fourier-domain analysis also has its limitations, and, as is shown later, both methods (Fourier-domain and space-domain) should be considered complementary rather than competitive.

III. BASIC EXPERIMENTAL CONSIDERATIONS

As was shown in the preceding section, the basic idea and the mathematics of DID-EPR are very simple. However, experimental imperfections can introduce limitations, the most serious of which are addressed below.

A. MAGNETIC-FIELD GRADIENT

The whole concept of deconvolution of the concentration profile is based on the assumption of linear mapping of x space onto B space. Any deviation of the gradient from uniformity along x violates this basic assumption and, thereby, at best, reduces the accuracy of the method.

B. SPATIAL SENSITIVITY OF THE SPECTROMETER

Variation of resonator sensitivity function, $S(x)$, over spatial dimensions makes the experiment "see" an effective concentration profile,

$$C_{eff}(x) = S(x)C(x) \qquad (14)$$

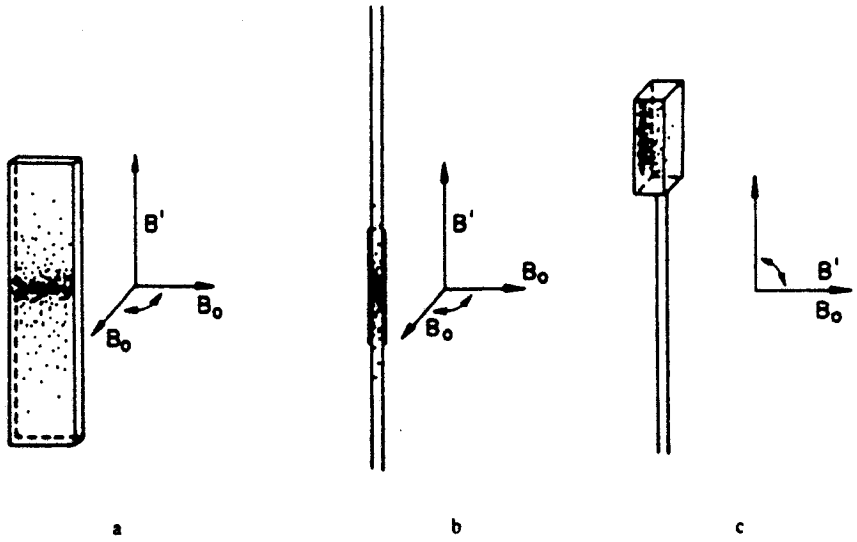

FIGURE 1. Schematic configuration of the sample for determination of diffusion coefficients in the unrestricted geometry of diffusion: (a) in model membranes (see Reference 34). (b) in liquid crystals, and (c) in the restricted geometry of diffusion in liquid crystals (see Reference 35).

and knowledge of S(x) is required. Once S(x) is known, the data can be analyzed in the space-domain without any problem,[31] but use of a Fourier-domain analysis is limited. Since $C_{eff}(x,t)$ is not the convolution of C(x,t) and S(x), there is no simple method of extraction of C(k,t) from $C_{eff}(k,t)$ in Fourier-space, even if we know the sensitivity of the cavity. Therefore, one can make most effective use of the Fourier-space analysis only if DID-EPR measurements are performed on concentration profiles extending over a distance limited to the center of the cavity, where S(ξ) is uniform.[32,34,35]

The necessity of working over very short distances emphasizes the importance of the preparation of as narrow initial distributions as possible. Narrow initial distributions have other virtues discussed below.

C. GEOMETRIES OF DIFFUSION

There are two simple and practical types of samples for the DID-EPR experiment. In the first one (I), a small amount of the spin-probe-enriched material is initially confined to the center of a quasi-1-D sample; in the case of liquid materials, the sample is prepared inside a capillary tube,[31,32] and, in the case of more viscous or solid materials (i.e., model membranes), a strip of a thin flat film of the pure material, sandwiched between glass plates, is used[32,34,37] (see Figure 1). Since, in this geometry, spin probes can diffuse in both directions from the source, it will be called the *unrestricted geometry* of diffusion.

In the second type of sample, (II) the initial distribution of spin probes is located at a reflective boundary, i.e., at the bottom or at the side-wall of the sample holder, see Figure 1. In this geometry, spin probes can diffuse only in one direction from the boundary, so we will call this case the *restricted geometry* for diffusion.

D. ACQUISITION OF SPECTRA

In standard EPR-spectroscopy, the spectrum is recorded by maintaining a constant microwave frequency and varying (sweeping) the magnetic field over some range, B_s, around the central-field value, B_o. This sweep always takes some time. In the preceding discussion, we have implicity assumed that the spectrometer permits an instantaneous detection of the EPR spectrum, particularly the I_s spectrum. Because the recording time (sweep time) is

finite, the above assumption is valid only as long as the spectrum can be considered time-independent over the time of sweep through the spectrum. Unfortunately, under standard experimental conditions, the sweep time may be sufficiently long to distort C(k,t). Such a distortion can lead to a significant systematic error in D_x.

Let the sweep rate be $v_s = \xi_s/t_s$, where t_s is the sweep time and ξ_s is the sweep range ($\pm \xi_s/2$ from the center) in units of the universal variable ξ. Then, by simple substitution, we find that the original Gaussian profile (see Equation 6) will be skewed by the recording procedure:[35]

$$\exp\left\{-\frac{1}{2}\frac{\xi^2}{\delta_\xi^2 + 2D_\xi t}\right\} \overset{\text{sweep}}{\Longrightarrow} \exp\left\{-\frac{1}{2}\frac{\xi^2}{\delta_\xi^2 + 2D_\xi t + (2D_\xi/v_s)\xi}\right\} \tag{15}$$

Because ξ changes sign, one half of the recorded curve is compressed, while the second half stretched with respect to the original Gaussian distribution, the degree of the distortion being inversely proportional to v_s. This effect may be thought of as the imaging analogue of the Doppler effect. If the distortion is not too large, i.e., $2D_\xi/v_s$ is small, the skewed profile can be approximated by

$$\begin{aligned}
&\exp\left\{-\frac{1}{2}\frac{\xi^2}{\sigma_\xi^2(t) + (2D_\xi/v_s)\xi}\right\} \\
&\quad \approx \exp\left\{-\frac{1}{2}\frac{\xi^2}{\sigma_\xi^2(t)}\right\} \cdot \left\{1 + \frac{1}{2}\frac{\xi^3}{\sigma_\xi^2(t)}\frac{2D_\xi}{v_s} + \ldots\right\} \\
&\quad \approx \exp\left\{-\frac{1}{2}\frac{\xi^2}{\sigma_\xi^2(t)}\right\} + \frac{D_\xi}{v_s\sigma_\xi^2(t)}\xi^3 \exp\left\{-\frac{1}{2}\frac{\xi^2}{\sigma_\xi^2(t)}\right\} + \ldots
\end{aligned} \tag{16}$$

where $\sigma_\xi^2(t) = \delta_\xi^2 + 2D_\xi t$, with t the time lapse since initialization of diffusion. The first term on the rhs is an even function and the second term an odd function of ξ. Thus, FT of Equation 16 would yield the Fourier-image of the first term in the real part and of the second term in the imaginary part of the transform, so only the real part should be used for analysis if the distortion of the concentration profile is significant. For small distortions, the variance of the skewed distribution is:

$$\begin{aligned}
\sigma_{\text{dist}}^2 &\approx [\delta_\xi^2 + (4 \ln 2)D_\xi^2/v_s^2] + 2D_\xi t \\
&= [\delta_\xi^2 + (4 \ln 2)D_\xi^2 t_s^2/\xi_s^2] + 2D_\xi t
\end{aligned} \tag{17}$$

as long as

$$2D_\xi t_s \ll \sigma_\xi^2 \tag{18}$$

The bracketed part of the rhs of Equation 17 is time-independent. Thus, as long as the broadening of the concentration profile due to the finite sweep time is small compared to the natural breadth of the profile, an artificial broadening caused by the sweep is approximately time-independent and small and, therefore, would not lead to a significant systematic error in determining D_x. Notice, at this point, that since the space available for diffusion is limited (by the cavity sensitivity) and t_s is usually fixed, condition Equation 18 sets the upper limit on the value of the diffusion coefficient one can determine with DID-EPR, as discussed in Section V.

Unfortunately, in the presence of a reflective wall, the finite sweep-time always has an influence on the estimated value of D_ξ, since one gets either the compressed, $\sigma^2(t)$, or the

stretched, $\sigma^2_-(t)$, profile depending on the direction of the sweep, $\sigma^2_-(t) < \sigma^2_+(t)$, leading to under- or overestimation of the diffusion coefficient, respectively. In principle, there is a possibility of repeating the measurement with the reverse direction of the sweep and averaging both results, but this can pose other technical problems requiring uniformity and equal sweep-rates in both directions as well as carefully aligned samples (see Section VI). Additionally, since the two sweeps cannot be performed simultaneously, they will be separated by the time of at least t_s, i.e., for the reflective wall in the center of the cavity one can measure either $\sigma^2_-(t)$ and $\sigma^2_+(t + t_s)$ or $\sigma^2_+(t)$ and $\sigma^2_-(t + t_s)$ depending on the direction of the first sweep; therefore, the averaging may, in fact, not improve the accuracy in D_ξ very much. Thus, instead of twin measurements with the sweep direction being changed in between, we find it preferable to reduce the systematic error of the one-way measurement to a minimum by shortening the sweep-time.

IV. NUMERICAL ANALYSIS OF THE DATA

The deconvolution of the concentration profile is done numerically via a discrete Fourier-transform (DFT), or more precisely, with the aid of the fast-Fourier-transform routine (FFT$^+$).[47] When using the DFT, all continuous FT used in the previous section are replaced by discrete sums. For example, DFT of $I_o(\xi)$ is

$$I_o(\kappa) = \sum_{\xi=0}^{N_s-1} I_o(\xi) e^{-2\pi j \xi \kappa / N_s} \tag{19}$$

where κ is now an integer from the range $(0,\ldots,N_s - 1)$. DFT of the other functions are defined in the same manner. The convolution equation (Equation 11) is replaced by the discrete convolution sum:

$$I_g(\xi,t) = \sum_{\xi' = -N_s/2+1}^{N_s/2} C(\xi',t) I_o(\xi - \xi') \tag{20}$$

It is important to remember that the discrete convolution theorem bears an explicit assumption that both functions being convoluted are periodic, with the periodicity of N_s, so there exists a possibility of unintentionally imposing a periodicity implied by the used of FFT$^+$ routines.

Once $I_g(\kappa,t)$ and $I_o(\kappa)$ are known, the (complex) concentration profile in the Fourier-domain $C(\kappa,t)$ can be calculated (see Equation 12). Up to this point the numerical manipulation of the data is the same for the space-domain and for Fourier-space, but procedures differ at a later stage (Section II).

A. SPACE-DOMAIN ANALYSIS

In the space-domain analysis, $C(\kappa,t)$ is subjected next to the inverse fast-Fourier-transform (FFT$^-$) in order to reconstruct the effective concentration profile $C_{eff}(\xi,t)$, see Equations 13 and 14. This has to be done in a special manner, however, to avoid numerical problems characteristic of the DFT deconvolution. Deconvolution can be unstable mathematically if the transform of the reference spectrum, (i.e., of $I_o(\kappa)$ is exactly zero or close to zero for some value (or values) κ, so that we cannot divide by it when calculating $C(\kappa,t)$.

$C(\kappa,t)$ therefore needs some sort of filtering prior to FFT$^-$ in order to remove these zeros. In the past, the optimal (Wiener) filter concept[47] was successfully implemented in the real-space analysis.[31]

$$C_{eff}(\xi,t) = \frac{1}{N_s} \sum_{\kappa=0}^{N_s-1} e^{2\pi j \kappa \xi / N_s} C(\kappa,t) \cdot W(\kappa) \tag{21}$$

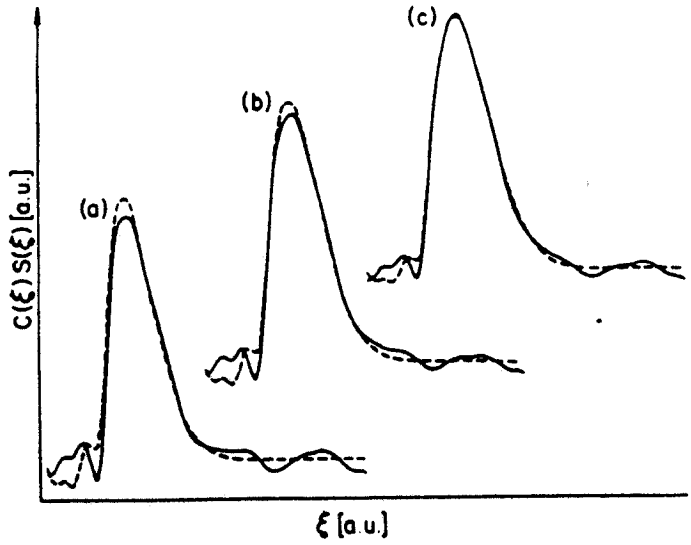

FIGURE 2. Effective concentration profiles of TEMPONE spin-probes diffusing in the nematic phase of 5, 4 at 300 K, along x-axis of the cavity: (–) deconvoluted using FFT⁻ and (----) the best fit of a Gaussian concentration-profile times the sensitivity of the cavity, S(ξ). Experimental profiles were recorded at different relative times (a) 2.2×10^4 s, (b) 9.7×10^4 s, and (c) 1.56×10^5 s. Variances of the fitted Gaussian profiles are (a) 0.186, (b) 0.284, and (c) 1.860 cm² (see Reference 31).

where $W(\kappa) = |I_g(\kappa,t)|^2/(|I_g(\kappa,t)|^2 + u)$, is the modified Wiener filtering function. $W(\kappa)$ effectively removes those regions most corrupted by numerical errors, if the constant u, which should be small and positive, is chosen properly. Furthermore, the results obtained using Equation 21 are quite insensitive to the value of u, although the function $W(\kappa)$ cannot be eliminated altogether.

$S(\xi)$ must be known in order to recover $C(\xi,t)$. With the help of Equation 8, by standard least-square minimization with respect to ξ^2, one can calculate the variance of the concentration profile, $\sigma_\xi^2(t)$,[31] see Figure 2. To determine D_ξ, the variance has to be known for at least two different t. However, to enhance the precision with which we determine D_ξ, it is advisable to use a series of $\sigma_\xi^2(t)$ measured for different t. Then, the least-square fit of $\sigma^2(t) = 2D_\xi t$ with respect to 2t yields D_ξ.

B. FOURIER-DOMAIN ANALYSIS

Analysis in the Fourier-domain does not require any further Fourier transforms, once $I_g(\kappa,t)$ and $I_u(\kappa)$ are known and, thus, should be considered not only simpler (recall that it does not depend on the particular shape of the initial concentration profile) but also faster and more precise.

Direct use of Equation 10 is not very convenient since it involves complex numbers. However, it is possible to simplify the analysis by taking advantage of the elementary properties of the Fourier transform and the properties of the transformed concentration profile.

The case of *unrestricted geometry* of diffusion is the simpler one. By expressing the complex concentration profiles $C(\kappa,t)$ in polar form, substituting into Equation 10, and equating the real parts and the imaginary parts, one gets:

$$\ln|C(\kappa,t)| = -2\pi^2\sigma_\xi^2(t) \cdot \kappa^2 + \ln|C(\kappa,t = 0)| \qquad (22)$$

Since any function can be written as the sum of an even and odd one, this can also be done with the initial concentration profile: $C_o(\xi) = {}^1/_2[C_o(\xi) + C_o(-\xi)] + {}^1/_2[C_o(\xi) - C_o(-\xi)] = C_o^e(\xi) + C_o^o(\xi)$. It is then easy to show from elementary properties of the Fourier transform that $C(\kappa,t) = \mathcal{R}eC_o^e(\kappa) \cdot e^{-2\pi^2\sigma_\xi^2(t)\kappa^2} + j\mathcal{I}mC_o^o(\kappa) \cdot e^{-2\pi^2\sigma_\xi^2(t)\kappa^2} = [A(\kappa) \cdot e^{j\phi(\kappa)}] \cdot e^{-2\pi^2\sigma_\xi^2(t)\kappa^2} = [A(\kappa) \cdot e^{-2\pi^2\sigma_\xi^2(t)\kappa^2}] \cdot e^{j\phi(\kappa)} = |C_o(\kappa,t)|e^{j\phi(\kappa)}$, i.e., all the important information about the concentration profile is indeed in the amplitude of $C_o(\kappa,t)$, and $\phi_t(\kappa) = \phi_o(\kappa)$, where $C(\kappa,t) = |C(\kappa,t)| \cdot e^{j\phi(\kappa)}$, i.e., all information about the time-development of the concentration profile is in the amplitude of $C(\kappa,t)$.

In the case of the *restricted geometry* of diffusion, the situation is different. Let us assume for simplicity that the (reflective) boundary is at $\xi = 0$. Then the solution of Equation 1 in the presence of the boundary condition, $\frac{\partial C}{\partial \xi}|_{\xi=0} = 0$, for the case of a point source placed at the boundary is also given by Equation 2, but with C_o now being replaced by $2C_o$ and ξ-space restricted to positive values.[44] Similarly, Equation 3 may also be easily adapted to this case.

Despite a similarity between Cases I and II, Fourier transforms of the concentration profiles are different, and this is due to the presence of the reflective wall. In principle, the boundary condition $\frac{\partial C}{\partial \xi}|_{\xi=0} = 0$ ensures that the concentration profile can be expanded only in Fourier-cosine series (and not Fourier-sine series) in the positive half of ξ-space. However, since the gradient-*on* spectrum is the convolution of the concentration profile with the reference spectrum (see Equation 20), the use of the Fourier transform to deconvolute this profile bears an *implicit* assumption that the mathematical function describing this profile is defined from $-\infty$ to $+\infty$ (continuous FT) or is periodic (DFT). It was not a problem for the unrestricted geometry of diffusion, but, in the case of the reflective boundary, $I_g(\kappa,t)/I_o(\kappa)$ has to contain information, not only about the concentration profile, but also about the discontinuity in this profile at $\xi = 0$ (or, in the case of DFT, periodically at $0, \pm N, \ldots$). Mathematically, this discontinuity can be thought of as the product of the even (real) function $C^e(\xi,t) = {}^1/_2[C(\xi,t) + C(-\xi,t)]$ and the unit step function. Conveniently for the Fourier transform analysis, it can alternatively be written as the sum of the (even and real) function $C^e(\xi,t)$ and the odd (real) function $C^o(\xi,t) = {}^1/_2[C(\xi,t) - C(\xi,t)]$, so the Fourier transform of $(C^e + C^o)$ will have a real part (the Fourier transform of C^e) and an imaginary part (the Fourier transform of C^o).[46] Note, most importantly, that the function $C^e(-\xi,t)$ is expandable in *exactly the same* cosine Fourier series as $C(\xi,t)$ but with ξ being allowed to also take on negative values. Therefore, full information about the time-development of the concentration profile in the presence of the reflective boundary is found in the real part of the recovered $C(\kappa,t) = I_g(\kappa,t)/I_o(\kappa)$. Equation 10 can then be replaced with

$$\ln \mathcal{R}eC(\kappa,t) = -2\pi^2\sigma_\xi^2(t) \cdot \kappa^2 + \ln \mathcal{R}eC(\kappa, t = 0) \tag{23}$$

In general, there are a number of different ways one can use Equations 22 or 23 to determine D_ξ.[32,34,35] The two most successful ones are as follows.

The concentration profiles recorded at different times are paired and then $\ln[C(\kappa),t_i)/C(\kappa,t_j)]$ are calculated. For convenience the authors continue to use $C(\kappa,t)$ although, in practice, it will be appropriately replaced by $|C(\kappa,t)|$ or $\mathcal{R}eC(\kappa,t)$. From Equation 10 it follows that

$$\ln\left[\frac{C(\kappa,t_i)}{C(\kappa,t_j)}\right] = -2\pi^2\Delta\sigma_{ij}^2\kappa^2 = -4\pi^2 D_\xi \Delta t_{ij}\kappa^2 \tag{24}$$

where $\Delta\sigma_{ij}^2 = \sigma_\xi^2(t_i) - \sigma_\xi^2(t_j)$ and $\Delta t_{ij} = t_i - t_j$. Then, in principle, a single least-square fit with respect to $\Delta t_{ij}\kappa^2$ of Equation 24 to experimental values of $\ln[C(\kappa,t_i)/C(\kappa,t_j)]$ gives D_ξ.

Data analysis in Fourier-space becomes even more convenient if one works with initial distributions that are narrow and quickly develop into a Gaussian, so it can safely be assumed at the time of measurement that the initial distribution was Gaussian with some variance, δ_ξ^2 and maximum value, C_o. Then from Equations 12, 10, and 7, we have

$$\begin{aligned} \ln C(\kappa,t) &= \ln\left[\frac{I_g(\kappa,t)}{I_o(\kappa)}\right] \\ &= -2\pi^2(\delta_\xi^2 + 2D_\xi t)\cdot\kappa^2 + \ln C_o \\ &= -2\pi^2\cdot\sigma_\xi^2(t)\cdot\kappa^2 + \ln C_o \end{aligned} \tag{25}$$

Thus, the least-square fit with respect to κ^2 of Equation 25 to experimental values of $\ln C(\kappa,t)$ yields $\sigma_\xi^2(t)$, and the diffusion coefficient can then be calculated from the slope of $\sigma_\xi^2(t)$ vs. $2t$. Note that since pairing is unnecessary in this case, this method should give better precision in the determination of D_ξ.

Propagation of experimental and numerical round-off errors introduces limitations to the Fourier-space analysis. These errors limit the number of κ values which are useful for analysis.[32,35] First, for sufficiently high κ, the magnitudes of the $C(\kappa,t)$ become very small (see Equation 25) and drop below the noise level. When these small numbers are the argument of the (natural) log, spurious values are obtained (see Equations 22 through 25). Cleary et al.[32] showed, by analysis of simulated concentration profiles with just numerical round-off errors due to single-precision FFT, that above a certain κ value the data becomes meaningless (see Figure 3). Second, because of experimental errors in $C(\kappa,t_i)$, the values of $\ln[C(\kappa,t_i)/C(\kappa,t_j)]$ are also corrupted at low enough κ such that differences between $C(\kappa,t_i)$ and $C(\kappa,t_j)$ are of the order of the random noise, especially when $(t_i - t_j)$ is small.[35] As a result of these limitations, linearity of $\ln[\frac{C(\kappa,t_i)}{C(\kappa,t_j)}]$, with respect to either κ^2 or $\Delta t_{ij}\kappa^2$, is observed over only a limited range of κ, $\kappa_{min} < \kappa < \kappa_{max}$. Estimation of D_ξ has, therefore, some degree of arbitrariness associated with the choices of κ_{min} and κ_{max}. To reduce this arbitrariness, the following simple procedure was proposed.[35] The diffusion coefficient is calculated from the data with different ranges of consecutive κ values taken into account. The calculated diffusion coefficient (D_{slope}) is then a function of the range of κ that is taken into account, (κ_{min}, κ_{max}). That is, $D_{slope} = D_{slope}(\kappa_{min}, \kappa_{max})$. However, these authors found[35] that if κ_{min} is small, D_{slope} is rather insensitive to its value. Then κ_{min} is set to a fixed small value, so D_{slope} becomes just a function of κ_{max}. For small values of κ_{max} ($\geq \kappa_{min}$), D_{slope} should initially have erratically scattered values. However, as κ_{max} increases it should go through a plateau corresponding to D_ξ. On further increase in κ_{max}, the scatter of data points at higher κ should force the D_{slope} to deviate (decrease) significantly again. Clearly, immediate advantages of such an analysis of calculated values of D_{slope} are (1) the removal of the aforementioned arbitrariness in choosing the cut-off limits for κ and (2) an instant read out of the D_ξ value from the plot.

One can estimate the uncertainty in D_{slope} (κ_{max}) as a function of κ_{max} in the following manner. One plots Equation 24 (up to κ_{max}) for the data from one pair of times t_i and t_j. This is repeated for all N/2 pairs. Then the plot D_{slope} (κ_{max}) is averaged over all pairs {i,j},[35,37] with standard deviation determined for each κ_{max}. The result is illustrated in Figure 4. D_{slope} goes through a plateau only over a limited range of κ-values, and, furthermore, the scatter of D_{slope} values is a minimum in that region. It is a significant advantage of the Fourier-domain vs. the space-domain analysis that D_ξ can be accurately determined even for a limited number of κ values.

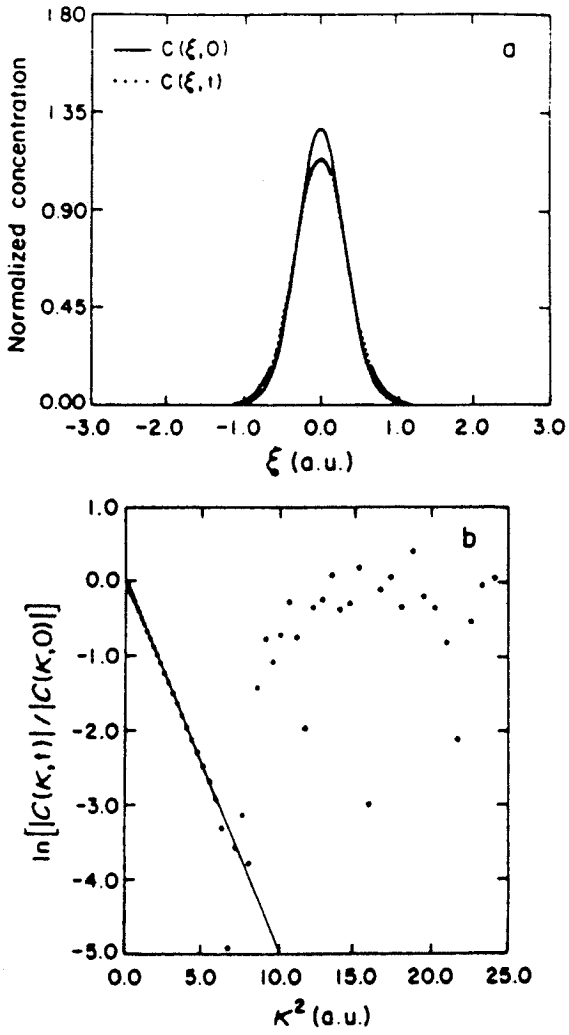

FIGURE 3. (a) Two Gaussian profiles, (—) $C(\xi, t = 0)$ and (...) $C(\xi,t)$, were generated on the computer ($D_x = 10^{-7}\,cm^2s^{-1}$ and $t = 10^3$ s) and subjected to FFT*; (b) a plot of $\ln\left[\frac{|C(\kappa,t)|}{|C(\kappa,0)|}\right]$ vs. κ^2 for these two profiles. Only about 30 κ values are useful for further calculations, corruption of the remaining κ values being due to the limited precision of the computer (single-precision).

V. LIMITS OF THE METHOD

In Table 1 the estimated limits of the DID-EPR experiment in different geometries are shown.[31,35] There are numerous potential sources of errors and limitations in the DID-EPR experiment, but, in what follows, attention is restricted to the most influential ones. The authors concentrate only on those effects which cannot be eliminated by careful tuning of the equipment and, therefore, are inherent to the experiment. Some of these effects are characteristic of EPR-spectroscopy in general, while the other can be associated with particular features of the DID-EPR experiment. The first group includes such obvious effects as the noise, nonuniform sensitivity of the cavity, or inhomogeneous static magnetic field.

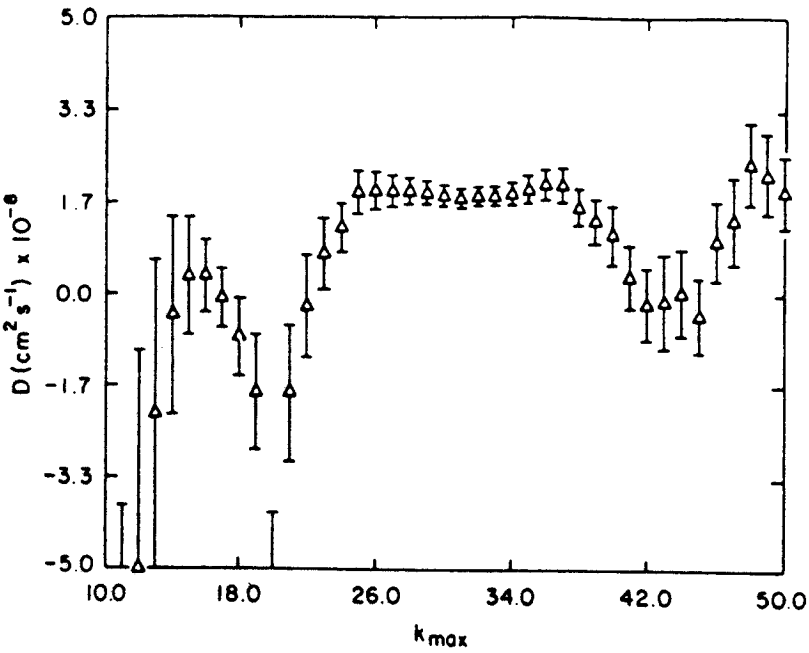

FIGURE 4. Average behavior of the D_{slope} as a function of κ_{max} for CSL diffusing in 1:1 POPC/DMPC (Reference 37). Nine pairs of $\tilde{I}_\xi(\kappa,t)$ were used in the calculations. Error bars correspond to the standard deviation of the average of nine points. Note that the plateau is also distinguished by a significant decrease in the random errors over the range.

To the second group belong such effects as a nonuniform magnetic-field gradient, finite sweep-time, poorly defined initial-concentration profile, or nonideal boundary conditions for diffusion. Some of these effects are mainly responsible for systematic errors; others cause random errors in D_x. This section will begin with the potential sources of the systematic errors, since they determine, first of all, the credibility of the DID-EPR technique.

Systematic errors manifest their presence predominantly in nonlinear behavior of experimental values of $\ln[\frac{C(\kappa,t_i)}{C(\kappa,t_j)}]$ as a function of κ^2 (see Equation 24). The principal sources of systematic errors are (1) nonuniformity of the field gradient, (2) position-dependent sensitivity of the cavity, and (3) finite sweep-time. These problems have already been mentioned in Section II so only the main conclusions will be reiterated here.

Since the cavity sensitivity $S(\xi)$ varies with position, the effective concentration-profile "seen" by the DID-EPR technique is the product $S(\xi) \cdot C(\xi,t)$. In the space-domain, this is not a big problem although it adds uncertainty to D_x;[31] however, in Fourier-space this leads to difficulty in the determination of D_x. In the latter case, a strongly inhomogeneous sensitivity would essentially exclude the possibility of a precise measurement of D_ξ altogether. If the variation of $S(\xi)$ is small, one has to expect a small, but systematic, deviation of the estimated value from the "true" one. The deviation can, to some extent, be compensated if the dependence of the sensitivity on position in the cavity is known;[35] however, the analysis is not an easy task and increases the uncertainty of D_ξ. Our experience with the narrow-flange TE_{102} X-band microwave-resonance cavity shows that the sensitivity of the cavity did not significantly influence results as long as the concentration profile was confined to $x_{max} \approx \pm 5$ mm around the center of cavity.

Similarly, the effect of a nonuniform gradient is extremely difficult to compensate or account for. Such a gradient would produce a nonlinear mapping of x-space onto B-space, violating the basic assumptions of the method (linear mapping), and, thereby, reduce the

TABLE 1
Range of D_x Measurable by DID-EPR

D_x [cm^2s^{-1}]	Space-domain	Fourier-domain	
		Rapid measurement	Delayed measurement
Lower limit[a]	$\sim 1 \cdot 10^{-6}$	$\sim 2 \cdot 10^{-9}$	$\sim 2 \cdot 10^{-7}$
Upper limit	$\sim 1 \cdot 10^{-3}$	$\sim 1 \cdot 10^{-5}$	$\sim 1 \cdot 10^{-5}$
Relative error	5—10%	1—10%	1—2%

[a] Canonical "1-h experiment". Lower values of D_x would require proportionally longer times.

accuracy of the method when distortions are small. Therefore, it is essential to frequently perform test measurements of the uniformity of the gradient.

The next substantial limitation results from the finite sweep time (see Section III.D). This has been shown to be significant in the case of restricted diffusion. However, the systematic errors caused by a finite sweep-time for restricted diffusion can be minimized by careful choice of sweep time. For example, if one wants sweep-related errors smaller than 2%, for an initial distribution width of 0.02 cm and D_x of order of 10^{-8} cm^2s^{-1}, the sweep-time should be faster than 0.05 s for a measurement performed shortly after initialization of the diffusion (rapid measurement) and faster than 50 s for a measurement with a concentration profile significantly broadened by the diffusion (delayed measurement). The FT-EPR technique discussed in Section VIII would be very useful in removing any effects due to finite sweep times.

At this point, the authors must emphasize that a combination of the restricted space available for diffusion and restrictions due to the finite sweep-time, set the upper limit on the measurable diffusion coefficient under given experimental conditions (see Equation 18). This limit was estimated (Table 1) from the broadest concentration-profile measurable, since such a profile guarantees the minimum error associated with the sweep-time under any circumstances. The maximum measurable breadth of the concentration profile is solely defined by the extent of the working region. These authors[35] suggested that the choice of the maximum measurable variance should be of the order of $(x^2_{max}/9)$. For concentration profiles with such variance, distortions from the sweep would be avoided if the diffusion coefficient obeys the inequality $2D_xt_s \ll (x^2_{max}/9)$ (see Equation 18) which, for example, for 60 s sweep-time gives $D_x \ll 2 \cdot 10^{-4}$ cm^2s^{-1}. It may then be anticipated that it should be possible to measure diffusion as fast as 10^{-5} cm^2s^{-1} with the unrestricted geometry of diffusion and with an initial distribution placed in the center of the cavity. However, when the reflecting wall is present, as a result of compressing or stretching the profile by the sweep, the maximum measurable diffusion-coefficients are smaller than this estimated limit. Note again the FT-EPR methods could be very helpful in eliminating this problem.

Even larger values of D_x can be measured in the space-domain experiment. In the practical realization of this experiment for measurements of fast diffusion, spin probes diffuse from a source placed just outside the cavity.[31] Again, because a standard EPR spectrometer is suitable for the measurements only over a limited distance around the center of cavity, favorable experimental conditions occur when a significant portion of the spin probes reach the central regions of the cavity. This happens when the variance of the concentration profile becomes of the order of the halfwidth of the cavity. For a narrow flange TE_{102} X-band cavity, this dimension is approximately 1.1 and 0.5 cm, in the X- and Z-directions, respectively. (These authors use X as the vertical axis, which is equivalent to the Y axis in Figure 1 of Chapter 3). With a sweep time of 60 s, the maximum measurable D_x in the space-domain experiment was estimated from Equation 18 to be of the order of 10^{-3} cm^2s^{-1}.

Due to the authors' interest in studying translational diffusion in liquid crystals and

model membranes, where typical diffusion coefficients are of the order of 10^{-6} to 10^{-10} cm^2s^{-1},[14,15] the primary concern was the lower limit of measurable D_x values. Until this point, all limitations mentioned arise from systematic errors inherent in the DID-EPR method. Random experimental errors, which are unavoidable in EPR spectra, are propagated by numerical manipulations, thereby introducing additional numerical round-off errors which limit the range of κ-values useful for analysis (see Section III). As a result, there is a limit on the minimum D_x which can be measured in a limited period of time, t_D. In Reference 6 we have shown that the lower and upper limits of the κ-range are estimated by

$$\kappa^2_{MAX} \approx \frac{\ln \epsilon_\kappa}{2\pi^2[\Delta_B^2 + (\sigma_\xi^2(t) + 2D_\xi t_D)]} \tag{26}$$

and

$$\kappa^2_{MIN} \approx \frac{1}{2\pi^2[(\epsilon_\kappa D_\xi t_D - \sigma_\xi^2(t)) - \Delta_B^2]} \tag{27}$$

respectively. Δ_B^2 is the variance of the EPR line (i.e., the rms width of a Gaussian EPR line in the absence of a field gradient), ϵ_κ is the signal-to-noise ratio in the Fourier-domain, and $\sigma_\xi^2(t)$ is the variance of the concentration profile at the beginning of the measurement. Equation 27 is physically meaningful as long as the denominator is positive, i.e., when:

$$D_\xi t_D > \frac{\Delta_B^2 + \sigma_\xi^2(t)}{\epsilon_\kappa} \tag{28}$$

One can analyze concentration profiles in the Fourier-domain in terms of Equation 24 only if $\kappa^2_{MAX} > \kappa^2_{MIN}$. From Equations 26 and 27, one gets

$$D_\xi t_D > \frac{\Delta_B^2 + \sigma_\xi^2(t)}{\epsilon_\kappa} \cdot \frac{1 + \ln \epsilon_\kappa}{\ln \epsilon_\kappa - 2/\epsilon_\kappa} \tag{29}$$

Again, the denominator of the second factor of rhs of Equation 29 has to be positive, i.e., $\epsilon_\kappa \ln \epsilon_\kappa > 2$, or $\epsilon_\kappa > 2.4$. Since under this condition the second factor is always greater than one, Equation 29 guarantees simultaneously the fulfillment of Equation 28.

Therefore, Equation 29 sets the lower limit for $D_x t_D$. For $\epsilon_\kappa \gg 2.4$ and using variables in x and B space, Equation 29 becomes:

$$D_x t_D > \frac{\Delta_B^2/B'^2 + \sigma_x^2(t)}{\epsilon_\kappa} \cdot [1 + 1/\ln \epsilon_\kappa] \tag{30}$$

Equation 30 sets the lower limit on the diffusion coefficient, which can be estimated in a given experimental time. A reasonable choice for a single measurement is an hour, $t_D \sim 1$ h. The authors' spectrometer, with usual "dynamic samples", yields an ϵ_κ of the order of 50, but the variance of the distribution can be anywhere between $\sigma_x(0) \approx 0.02$ cm and $\sigma_x(t) \approx (X_{max}/3)$, where the lower limit is defined by the breadth of a narrow initial distribution, and the upper limit corresponds to the size of the sensitive region in the center of cavity.[31-37] These limits correspond to two principal applications of the DID-EPR experiment. The first one is for a rapid DID-EPR measurement, which, for best results, should be performed as soon as possible after initialization of the diffusion. The variance of the concentration profile is then essentially equal to that of the initial distribution. The second

type of application is in a multiple measurement on the same sample, e.g., temperature-dependent studies, when the last measurement is usually performed on a very broad sample. Usually the EPR lines are narrow, say $2\Delta_B \approx 0.5$ G, so the term Δ^2_B/B'^2 in Equation 30 can be omitted. Then, for a 1-h measurement, ($t_D \approx 4000$ s) performed in these two limiting cases, Equation 30 yields $D_x > 2 \cdot 10^{-9}$ cm^{2}s^{-1} for the rapid measurement and only $D_x > 2 \cdot 10^{-7}$ cm^{2}s^{-1} for a delayed one. The latter limit restricts, therefore, a multiple measurement to cases when the diffusion coefficient is of the order of 10^{-7} cm^{2}s^{-1} or higher. The situation worsens, however, if the EPR line is broader. For $\Delta_B \approx 2$G and $B' = 100$ Gcm^{-1} (rapid measurement), $D_x > 4 \cdot 10^{-9}$ cm^{2}s^{-1} is obtained, and for $B' = 10$ Gcm^{-1} (delayed measurement), $D_x > 4 \cdot 10^{-7}$ cm^{2}s^{-1} is expected.[35] Therefore, it is crucial to use spin probes with very narrow EPR lines for studying very slow diffusion processes.

In summary, the "1-h" space-domain experiment is particularly suitable for measuring diffusion coefficients in the range 10^{-5} cm^{2}s^{-1} < D_x < 10^{-3} cm^{2}s^{-1}, while the "1-h" Fourier-domain experiment should be used to study diffusion coefficients in the range 10^{-9} to 10^{-7} cm^{2}s^{-1} < D_x < 10^{-5} cm^{2}s^{-1}.

The precision of the DID-EPR experiment is also important. Detailed discussion of the propagation of random errors is given elsewhere.[35] It was found that for a typical signal-to-noise ratio of $\epsilon_n \approx 50$ and standard experimental conditions (see Section VI for details), the standard deviation for D_x should be of the order of 10^{-10} cm^{2}s^{-1}. This corresponds to relative errors in D_x to be 10 to 20% for diffusion coefficients of the order of 10^{-9} cm^{2}s^{-1}, but below 1% for 10^{-7} cm^{2}s^{-1}. For fast diffusion-processes, errors arising from uncertainties in B' and B_s give a substantial contribution to the error in D_x.

Although the estimated error in D_x is valid in both unrestricted and restricted geometries, the reader must be aware of additional errors resulting from imperfections of the reflective-wall surface (nonuniform boundary conditions at the wall).[35] It was estimated that the errors due to the roughness of the reflective wall increase the uncertainty of D_x from below 1% to a few percent in the presence of the wall. To minimize the uncertainty of D_x in this case, it is very important to use very good quality (flat) reflecting-wall surfaces, perfectly oriented with respect to the direction of the gradient.

As a conclusion to this section, the authors note that since the working region is limited, the total number of measurements which can be done on the same sample depends heavily on the diffusion coefficient. For example, it was found[35] that for D_x of the order of 10^{-7} cm^{2}s^{-1}, it should be possible to perform $n \approx 6$ measurements on the same sample, but for 10^{-6} cm^{2}s^{-1}, $n \approx 2$. This prediction is in good agreement with our experimental findings during temperature-dependent studies of the translational (and rotational) diffusion in model membranes.[34,37]

VI. NUTS AND BOLTS OF THE DID-EPR EXPERIMENT

The present section is primarily devoted to a description of the essential components of the instrumentation and of experimental and numerical procedures of standard DID-EPR experiments, as the authors have implemented them in their laboratory.

A. INSTRUMENTAL

In this paragraph, the main components and parameters for the experimental arrangement are reviewed.[32-37] The DID-EPR experiments are carried out on a standard EPR spectrometer. These measurements have been performed at X-band in either a Varian model E12 or Bruker model ER-200D spectrometer,[31-34] with a TE_{102} narrow-flange microwave cavity. The standard first-derivative mode—with 100 kHz modulation and microwave powers of about 5 mW (Fourier-domain) and 10 mW (space-domain)—is used for recording spectra. The modulation amplitude is kept the same for the gradient-on and gradient-off spectra. A typical

signal-to-noise ratio during DID-EPR experiments is approximately 50. A convenient sweep range (B_s) is 100 G.

The most important part of the DID-EPR experiment is a system generating a linear magnetic-field gradient across the cavity. In the past, homemade[31-34] and commercial[32,35,37] coils, as well as a pair of matched ferromagnetic wedges,[32] were used. Currently, a pair of George Associates Lewis Coils, model 502, are employed. Each of the Lewis Coils consists of a figure-eight coil. By appropriate connections between the electric terminals of each half of the figure-eight coils, the coils can provide uniform field gradients either parallel or perpendicular to the main static field, with gradient uniformity better than 0.2% over 1.0 cm in the center of the cavity. The magnitude of the field gradient can be continuously changed by varying the current through the coils.

The Lewis Coils are currently driven by a Sorensen DC Power Supply, either model DCR150-10A or SRL20-25. Typically, when connected for the parallel-field gradient, the Lewis Coils produce a gradient of 200 G/cm at a current of about 10 A. For the perpendicular arrangement, the gradient is 100 G/cm at a current of 15 A.

Data from the Varian E12 are collected on a Leading Edge model D PC interfaced to an HP 3457 multimeter. The multimeter monitors the analog signal going to the XY-recorder of the EPR spectrometer. All spectra are digitized to 1024 points. (On the Bruker ER-200D, the spectra are collected on an IBM 9000 via a Data Precision waveform analyzer model Data 6000.)

To image along the x axis of the cavity, one utilizes standard sample mounts and a temperature controlling Dewar for the cavity. For imaging along the z axis, some modifications are required. The space-domain experiment requires special modification of the sidewalls of the TE_{102} cavity to contain two chimneys.[31] The Fourier-domain experiment in the unrestricted geometry requires the use of a TM cavity; however, in the restricted geometry of diffusion, the standard sample mounts, and a temperature-controlling system can be used with a TE_{102} cavity.[35]

B. EXPERIMENTAL PROCEDURE (FOURIER-DOMAIN)

Typical samples for the space-domain and Fourier-domain experiments are shown schematically in Figure 1. Preparation of a sample for 1-D diffusion depends on the nature of the material in which spin probes are going to diffuse; the reader should refer to References 31 to 34 for details.

A detailed description of the experimental procedure in the space-domain and in the Fourier-domain can be found in References 31 and 32. Since they are very similar, for simplicity the concentration here is on the case of the Fourier-domain experiment which, the authors believe, will be in more frequent use in the future.

Immediately after preparation, the sample is located in the center of the cavity. Since random errors present in the EPR spectra limit the range of κ values for analysis, prior to recording the gradient-on spectra the magnetic-field gradient must be optimized for the maximum range of κ. We optimize the measurement by maximizing the difference $(\kappa^2_{MAX} - \kappa^2_{MIN})$. There are two independent variables in Equations 26 and 27 (see Section V), t_D and B'^2, so one can either optimize t_D for a single measurement (fixed magnetic-field gradient) or optimize the magnetic-field gradient during multiple measurements since then t_D is essentially fixed. In the latter case, using the usual criterion for the extrema of $(\kappa^2_{MAX} - \kappa^2_{MIN})$, one gets with the help of Equations 26 and 27

$$\frac{B'^2}{\Delta_B^2} = \left[\sqrt{\frac{\alpha}{\beta \ln \epsilon_\kappa}} + 1\right]\left[\alpha - \sqrt{\frac{\alpha\beta}{\ln \epsilon_\kappa}}\right]^{-1} \tag{31}$$

where $\alpha = \epsilon_\kappa D_s t_D - \sigma_s^2(t)$ and $\beta = 2D_s t_D + \sigma_s^2(t)$. Note that Equation 31 has a physical

solution only if $\alpha > 0$, i.e., $D_x > \sigma_x^2(t)/(\epsilon_x t_D)$. This condition is already guaranteed by Equation 30. For $\epsilon_x = 50$, $t_D = 4000$ s, $D_x = 10^{-8}$ cm^{2}s^{-1} and $\sigma_x^2(t = 0) = (0.01$ cm$^2)$ (initial concentration profile), one obtains from Equation 31 the optimum $B'^2/\Delta_B^2 \approx 40$ cm^{-2} which is in fairly good agreement with the gradients used in practice (80 to 100 G/cm).

Once the optimum gradient is set, the progress of the diffusion is monitored in the following manner. A series of N consecutive gradient-on spectra, $I_g(\xi,t)$, ($N \sim 10$) are collected as frequently as possible, effectively every 100 to 200 s; later, the concentration profile is allowed to develop over a period of $t_D = 2000$ to 4000 s, and the series of N measurements is repeated again. Thus, the whole set consists of 2N spectra.

The next step after obtaining the gradient-*on* spectra depends on the geometry of the experiment. In the *unrestricted geometry* of diffusion, since only the amplitudes of $C(\kappa,t)$ are needed (see Equation 22), it is easy to show that in Equation 24 $C(\kappa,t)$ can be replaced by $|I_g(\kappa,t)|$, i.e., knowledge of the gradient-off spectrum is unnecessary.[32,35] The case of the restricted geometry of diffusion situation is more complicated, since we need $\mathfrak{Re}C(\kappa,t)$ in Equation 24, and to compute these numbers, the reference spectrum is required. However, an additional problem arises, since usually the reflecting wall and/or the reference spectrum are displaced along ξ as a result of switching the gradient on and off. To understand this difficulty, first consider the fact that the EPR spectrum is recorded only over limited sweep range (i.e., $\pm\frac{\xi_s}{2}$) around the center value of ξ_o. Thus, the particular position of the EPR spectrum inside this "window" depends on the value of ξ_o. The spectrum recorded in the absence of the gradient is the reference one (I_o), and we may consider ξ_o as the reference point of this spectrum (origin) on the ξ-scale. (Recall that ξ_o corresponds to the value of main static field.)

When the magnetic-field gradient is switched-on, the static magnetic field at the position of the reflecting wall will, in general, change because of the gradient (i.e., by an amount of ξ'), so there is a mismatch between the position of the reflective wall ($\xi_o + \xi'$) and the reference point (ξ_o) on the ξ-scale. Consequently, the gradient-on spectrum is the convolution of the concentration profile and the shifted reference spectrum. Therefore, the corresponding Fourier transform contains a κ-dependent phase-factor contributing to the real and imaginary parts of $I_g^d(\kappa,t)$: $I_g^d(\kappa,t) = C(\kappa,t) \cdot I_o(\kappa)e^{2\pi\kappa\xi'\kappa}$, ξ' is the displacement between $C(\xi,t)$ and $I_o(\xi)$, and the superscript d refers to the displaced functions. Thus, to extract $\mathfrak{Re}C(\kappa,t)$ both real and imaginary parts of C^d have to be taken into account, and Equation 24 takes the form of

$$\ln\left\{\frac{\cos\kappa\xi' \cdot \mathfrak{Re}C^d(\kappa,t_i) + \sin\kappa\xi' \cdot \mathfrak{Im}C^d(\kappa,t_i)}{\cos\kappa\xi' \cdot \mathfrak{Re}C^d(\kappa,t_j) + \sin\kappa\xi' \cdot \mathfrak{Im}C^d(\kappa,t_i)}\right\} = -4\pi^2 D_\xi t\kappa^2 \qquad (32)$$

where $C^d(\kappa,t) = I^d(\kappa,t)/I_o(\kappa)$. Since ξ' is the relative mismatch between the positions of the wall and of the center of the reference spectrum, the phase-factor can be interpreted as resulting from either shifting the reflective wall or the reference spectrum. Experimentally accounting for ξ' through Equation 32 cannot be accomplished easily, so alignment of the reflecting wall with the reference spectrum is advisable.[32,35]

To perform a successful deconvolution of the concentration profile one has to check for, and, ultimately, counteract the mismatch prior to FFT$^+$. These corrections can be performed by adjustments in x-, B-, and ξ-spaces, since they are formally equivalent. To make a proper adjustment, we need a reliable method of controlling "alignment". The principles of monitoring the alignment of the spectra are described in Reference 31. Most frequently, an EPR spectrum is detected as the first derivative of the absorption, which can be written as[35]:

$$I_g(\xi) = \frac{dI_g}{d\xi} = C(0)I_o(\xi) + \int_0^\infty \frac{dC(\xi')}{d\xi'} I_o(\xi - \xi')d\xi' \qquad (33)$$

where it is assumed that the reflective wall is present at $\xi = 0$. Assume for a moment that $I_o(\xi)$ is a singlet. Then, because $dC/d\xi$ is either zero or very small (negative) in value in the vicinity of the reflecting wall (recall the boundary condition, $\frac{\partial C}{\partial \xi}|_{\xi=0} = 0$), the first term on the rhs, which is just the absorption line scaled by the factor C(0), dominates the spectrum around $\xi = 0$. Therefore, this (sharp) maximum corresponds to the position of the reflective wall on the ξ-scale. Similarly, for a double- or triple-line reference spectrum, like ^{15}N or ^{14}N nitroxide spin-labels, as a result of the presence of the reflective boundary, $I'_g(\xi)$ should feature maxima uniquely corresponding to the reference spectrum lines. To eliminate the phase factor in Fourier-space, both spectra, I'_g and I_o, have to be aligned in a such way that positions of sharp maxima in I'_g coincide with the crossover points in I'_o.

This alignment can be achieved in x-space by varying the position of the reflective wall inside the cavity,[32] or in B-space by changing the static magnetic-field between recording I'_g and I'_o, or, finally, in ξ-space by numerical shifting of the spectra.[35] The first-derivative spectra of gradient-on and gradient-off should first be recorded, and their positions on the recording chart compared. If they do not match, adjustment is necessary. First, one can repetitively move the position of the reflective wall inside the cavity, record I'_o, and then recheck if satisfactory alignment has been achieved. Alternatively, one can obtain alignment by just varying the position of I'_o through changes of the static magnetic-field. It is, however, very difficult to judge when the alignment is satisfactory. At this point, the D_{slope} vs. k_{max} plot comes to our rescue. In the case of a perfect match between the spectra, D_{slope} goes through a plateau over the (k_{MIN}, k_{MAX}) range, the D_{slope} value at the plateau corresponding to D_x, the same way it does for the unrestricted diffusion experiment, Figure 4. In the presence of a mismatch between spectra, a k-dependent phase factor appears in C(k,t), and the plateau disappears even for a very slight displacement, see Figure 5a.

If the recorded $I'_o(\kappa)$ spectrum does not produce a reliable plateau, further adjustments are possible by a careful numerical shift of the $I'_o(\xi)$ spectrum along the ξ-axis. The results of such manipulations of the experimental data from Figure 5a are shown in Figure 5b. Clearly, it was possible to adjust all reference spectra and to obtain essentially the same plateau. (Notice fluctuations in D_{slope} resulting from a nonideal boundary at the wall.)

C. NUMERICAL CALCULATIONS

Various numerical procedures for data analysis were investigated in the past.[31-37] Numerical procedures for the space-domain experiment can be found in the work of Hornak et al.,[35] while those for the Fourier-domain experiment were discussed in full in References 32 through 35. Below, an outline of the algorithm the authors find the most reliable and universal in Fourier-space is presented. The procedure is based on the pairing of concentration profiles and subsequent use of Equation 24. The typical procedure is as follows: (1) All $I_g(\xi,t_i)$ and $I_o(\xi)$ spectra are subjected to FFT* to obtain $I_g(\kappa,t_i)$ and $I_o(\kappa)$. (To avoid the wraparound problems of FFT,[47] each spectrum prior to FFT was zero-padded beyond the last point to a total of 2048 points). (2) $I_g(\kappa,t_i)$ spectra are paired: {j,N/2 + j}, j = 1,..., N/2, so there are N/2 pairs. (3) Each data pair is analyzed in terms of a linear least-square fit to Equation 22 (unrestricted geometry) or Equation 23 (restricted geometry) with respect to $\Delta t_{ij}\kappa^2$ over a variable range of κ values, with κ_{min} fixed and κ_{max} varied, see Section IV.B. As a result, D_{slope}, averaged over N/2 pairs, is calculated as a function of κ_{max}. This averaging can be done in two slightly different manners which lead to the same result; either the linear least-square fit is performed on all pairs of data simultaneously,[35] or each pair is analyzed independently and only then are all $D_{slope}(k_{max})$ curves averaged.[37] A typical result

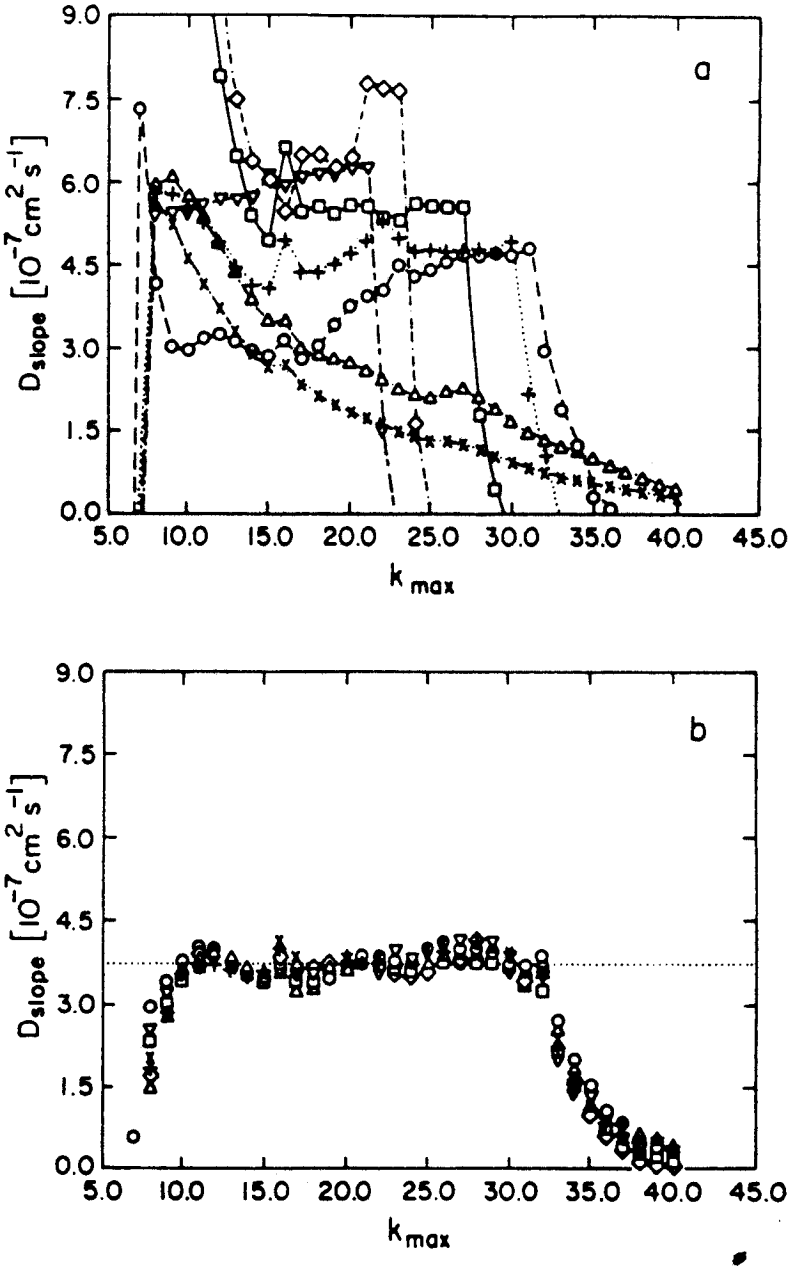

FIGURE 5. Typical behavior of $D_{slope}(k_{max})$ in the presence of a reflective wall calculated for a number of $I_o(B)$ spectra slightly (but differently) displaced with respect to the $I_\xi(B,T)$: (a) without numerical adjustment of the alignment, (b) the same data but after numerical adjustment; dotted straight line indicates the average value of D_{slope} at the plateau.

of the latter analysis is shown in Figure 4. (4) The value of D_ξ is determined as the value of D_{slope} at the plateau, and D_x is calculated by rescaling ξ-space back to x-space: $D_x = D_\xi/B'^2$.

VII. APPLICATION OF DID-EPR TO LIQUID CRYSTALS AND MODEL MEMBRANES

In the course of the development of the DID-EPR technique, the authors have performed

TABLE 2
Translational Diffusion Constants Measured by DID-EPR*

Host material	Probe	Temperature (K)	D(cm^2s^{-1})
H_2O	TEMPONE	295	1.7×10^{-5}
C_2H_5OH	2,5-DTBSQ	295	2.7×10^{-5}
5,4 (iso)	TEMPONE	323	2.5×10^{-6}
5,4 (nem) D⊥	TEMPONE	300	9.0×10^{-7}
5,4 (nem)D∥	TEMPONE	300	6.4×10^{-7}
MBBA (nem)D⊥	^{15}N-PDT	293	2.5×10^{-7}
MBBA (nem)D∥	^{15}N-PDT	293	3.7×10^{-7}
Phase V (nem)D⊥	TEMPONE	294	1.25×10^{-7}
Phase V (nem)D⊥	OBSL	294	0.48×10^{-7}

Note: TEMPONE = 2,2,6,6-tetramethylpiperidine-1-oxyl; 2,5-DTBSQ = 2,5-di-tertiary-butyl-para-benzosemiquinone; 5,4 = *p*-pentylbenzylidene-*p*-butylaniline; MBBA = *p*-methoxybenzylidene-*p*-butylaniline; ^{15}N-PDT = PD-TEMPONE (^{15}N-labeled); Phase V = nematic mixture; OBSL = octylbenzoyl spin label.

* [Added in proof: Extensive measurements as a function of temperature have been made of $D_\parallel$ and $D_\perp$ for both PDT and CSL in a smectic liquid crystal called™ S2 (Moscicki, J. K., Shin, Y. K., and Freed, J. H., to be published)].

several measurements on some isotropic liquids and thermotropic nematic liquid-crystals[30-32,35] at or near room temperature.

A summary of translational diffusion coefficients that the authors have measured by DID-EPR appears in Table 2. It is interesting to note, that *p*-methoxybenzylidene-*p*-butylaniline (MBBA) and *p*-pentylbenzylidene-*p*-butylaniline (5,4) show opposite types of diffusional anisotropy. Whereas, for MBBA $D_\parallel > D_\perp$, which is typical behavior for the nematic phase,[14] the result that $D_\parallel < D_\perp$ for 5,4 suggests some smectic-like character of the nematic phase of this compound, an interesting finding in the light of studies of molecular dynamics at the smectic-nematic phase transition currently underway in the authors' laboratory.[48]

An excellent example of the applicability of DID-EPR to detailed studies of molecular dynamics is offered by the authors' investigations of the effects of cholesterol on the dynamics and the structural properties of two different spin probes, the sterol-type CSL and the phospholipid-type 16-PC in phospholipid/cholesterol (POPC/cholesterol or DMPC/POPC/cholesterol; POPC refers to 1-palmitoyl-2-oleoyl-*sn*-glycero-phosphatidylcholine and DMPC to 1,2-dimyristoyl-*sn*-glycero-phosphatidylcholine)-oriented multilayer model-membranes.[34,35,37] Due to the relatively small translational diffusion-constants of these spin labels in the model membranes ($\sim 10^{-8}$ cm^2s^{-1}), multiple measurements of the translational diffusion coefficient, D, on a single sample were performed (see Figure 6). Furthermore, by analyzing the gradient-off spectra collected in the course of the DID-EPR experiment, the order parameter, S, and the rotational diffusion constant, $R_\perp$, utilizing EPR spectral-stimulation methods, were also simultaneously obtained.[42,43] Since spin probes were chosen purposely to mimic either cholesterol (CSL) or (16-PC) behavior, this enabled in-depth considerations of the effects of the membrane composition and temperature on the dynamic molecular structure of the membranes. Remarkable correlations for both types of molecules (viz. lipid and cholesterol) were found. In each case one obtains the form $D_\perp = D^0_\perp \exp[-E_a(x,T)/RT]$ where the activation energy is $E_a(x,T) = \alpha(T)S^2(x,T) + \beta$ and $\alpha T = a + b/T$ (see Figure 7). Similar correlations were found between $R_\perp$ and S both as a function of the mole fraction of cholesterol x and temperature T in the liquid-crystalline phase. This provides clear demonstration that the model membranes are simple nonideal solutions.[33,34,37] In POPC/cholesterol solutions, very substantial variations of D,R$_\perp$, and S for CSL (as x is

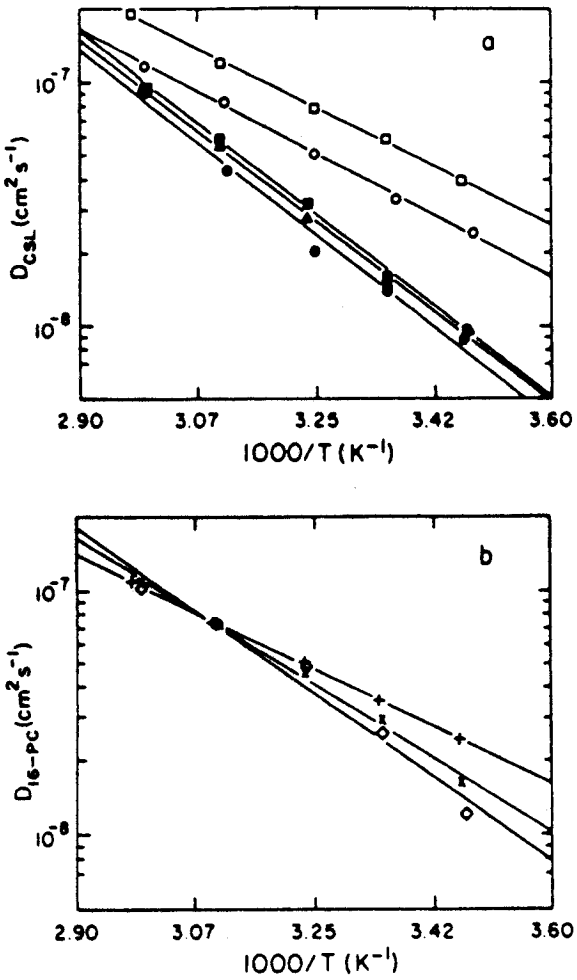

FIGURE 6. Translational diffusion of (a) CSL and (b) 16-PC spin probes in POPC/cholesterol model membranes (Reference 34). Semilog plots of the diffusion coefficient as a function of temperature for different concentrations of cholesterol. Cholesterol concentrations are (a) 0 (□), 4 (○), 10 (△), 20 (■), and 30 mol%(●) and (b) 0 (+), 10 (×), and 20 mol% (◇).

increased from zero) were observed, whereas only modest changes were observed for 16-PC.[33,34] These authors' results demonstrate the preferential association of cholesterol molecules (including CSL) with each other in POPC solvent. As a result, the environment of CSL changes significantly as a function of x, from that of flexible POPC molecules, to the more rigid cholesterol molecules, which is manifested by a decrease of both D and $R_\perp$ with increasing x. On the other hand, the tendency of cholesterol to aggregate means that the POPC-rich regions are less influenced by cholesterol molecules than would otherwise be expected. This is consistent with the rather modest effect of cholesterol on the lateral diffusion of 16-PC. Experiments with CSL spin-label in DMPC/POPC/cholesterol ternary mixtures show a weaker effect of cholesterol on D, indicating that addition of the saturated lipid DMPC to the unsaturated lipid POPC enhances the mixing of cholesterol in PC model membranes.[37]

Aside from liquid-crystal and model-membrane studies, one may expect to investigate polymers, e.g., rod-like lyotropic polymer liquid crystals, which demonstrate unique mo-

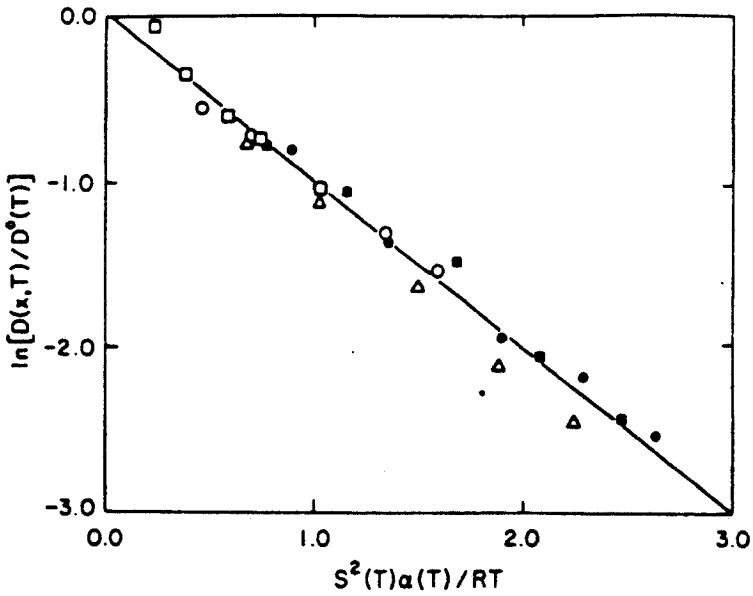

FIGURE 7. Translational diffusion of CSL spin probe in POPC/cholesterol model membrane (Reference 34). Universal behavior of the diffusion coefficient as a function of the order parameter and temperature is displayed. Cholesterol concentrations are 0 (□), 4 (○), 10 (△), 20 (■) and 30 mol% (●), and $\alpha(T) = a + bT$.

lecular dynamics.[49-52] Existing data on rotational molecular dynamics in these systems suggest that one should expect very strong coupling between the rotational and translational motions of rod-like macromolecules. Theories of molecular dynamics in semidiluted solutions of rods predict a very strong dependence of diffusion constants on the elongation of macromolecules and their concentration.[53,54] In particular, dramatic changes can be anticipated at the nematic-isotropic phase transition. DID-EPR of spin-labeled macromolecules together with EPR rotational-dynamics studies would help to verify such theories. Additionally, by using small spin probes, it is possible to study the interactions between the solvent and solute molecules, interactions which play an important role in the formation of the liquid-crystalline state.[50] The authors anticipate the translational diffusion to be sufficiently slow (approximately $\sim 10^{-7}$ to 10^{-9} cm^2s^{-1}) to enable multiple use of a single sample.

Another potential application of the DID-EPR method is to the measurement of rates of reduction of spin probes if lineshape does not change at different positions. Detection and monitoring of inhomogeneous concentration profiles of spin probes undergoing diffusion and reduction at the same time might be especially important in medicine and technology, for example, for studying areas of altered physiology (which would be expected to exhibit different types of metabolic rates and processes), or reaction of tissues to different drugs (spin labeled), on the one hand, and for studying oxidative degradation of polymers through monitoring diffusion of the O_2 from the surface into bulk polymer, on the other hand.

Schara and coworkers[25] first used the EPR-imaging method to study diffusion in the presence of reduction of nitroxides in biological tissues, not by deconvolution of the concentration profile, but by simulation of the spectrum from an idealized concentration profile. They suggest that reduction of nitroxides by cells follows first-order kinetics, i.e., the concentration of the spin probes is controlled by:

$$\frac{\partial C(x,t)}{\partial t} = D\frac{\partial^2 C(x,t)}{\partial x^2} - r_1 C(x,t) \qquad (34)$$

where r_1 is the first-order reduction constant. However, at the inital stages, the reduction of spin labels proceeds very rapidly compared with the diffusion process, and local equilibrium can be assumed to exist between free and reduced spin-labels. They found that at the initial stages the equation of diffusion becomes:

$$\frac{\partial C(x,t)}{\partial t} = D\frac{\partial^2 C(x,t)}{\partial x^2} - \frac{\partial r_o C(x,t)}{\partial t} \tag{35}$$

due to the local equilibrium, i.e., concentrations of reduced and free spin-labels are proportional to each other, $C_r = r_o C$.

Note that the DID-EPR technique offers, in principal, a much more convenient way of measuring both D and the reduction-rate constants. It follows directly from Equation 35 that, in the case of the rapid reduction of spin probes, the diffusion constant would be lowered by just the factor $1/(1 + r_o)$. If first-order reduction is involved, our basic equation, Equation 24, takes the form:

$$\ln\left[\frac{C(\kappa,t_i)}{C(\kappa,t_j)}\right] = -4\pi^2(D_\xi\kappa^2 + r_1)\Delta t_{ij} \tag{36}$$

Therefore, if one plots $\ln[\frac{C(\kappa,t_i)}{C(\kappa,t_j)}]$ vs. κ^2, the slope $-4\pi^2 D_\xi \kappa^2 \Delta t_{ij}$ depends only on the diffusion constant, while the intercept $-4\pi^2 r_1 \Delta t_{ij}$, only depends on the rate of reduction. Thus, both quantities are easily determined by respectively plotting the slope and the intercept as a function of Δt_{ij}.

VIII. RECENT AND FUTURE DEVELOPMENTS IN EPR IMAGING OF DIFFUSION

Despite the fact that the DID-EPR technique developed substantially, one should be able to improve it further. For example, there are several ways one can enhance the signal-to-noise ratio, S/N. These include the use of a low-noise microwave GaAsFET preamplifier such as is commonly employed in modern time-domain EPR spectrometers.[55] A loop-gap resonator, which has a very high filling factor and very good spatial homogeneity of the sensitivity, could also be used.[56] Once this is accomplished, the sweep time could be reduced and higher gradients applied, thus improving the precision (by increasing $\kappa^2_{MAX} - \kappa^2_{MIN}$) and shortening the overall experimental time (see Equations 26, 27, and 30). Next, one could work with narrower and better-defined initial distributions. To work with better initial distributions, new techniques of preparing the initial distribution must be explored. One possible way of generating a fine initial profile is to use spin-label photoproduction by either photodissociation (pd) or photoionization (pi)[57] or their photoreduction (pr).[58] Photoreduction was once used by Sheats,[18] although not in an imaging experiment, and it has been proven a useful technique for producing an inhomogeneous gradient of spin probes.

The EPR imaging of dynamic samples has been studied in other laboratories.[23,28] Berliner and his colleagues[23] are developing a technique for studying diffusional processes in biological tissue. Their method is based on the reconstruction of a two-dimensional (2-D) image of the concentration profile from the spectra recorded with the aid of a flat-loop surface coil at L-band (1.6 GHz). A model study of translational diffusion of 4-hydroxy-2,2,6,6-tetramethylpiperidine-1-oxyl (TEMPOL) spin-probe into a cylindrical polyacrylamide gel containing lossy electrolyte solution was performed, and the diffusion coefficient calculated. This is important for potential application of EPR imaging to biological samples, i.e., their result suggests that it should be feasible to apply this method to real "lossy" biological samples from which one may obtain *in vivo* diffusion coefficients.

The Eatons and their co-workers[28,29] have shown how the complete EPR spectrum may be obtained as a function of location in a sample in which the spin probe is undergoing transport. This method is referred to as spectral-spatial EPR imaging. This method expands the range of cases for which EPR imaging can yield diffusion and other transport information. For example, in principle, one can study the microscopic diffusion coefficients from HSE broadening[30] and the macroscopic diffusion coefficients from DID-EPR simultaneously. [Added in proof: This has now been realized (Shin, Y. K., Ewert, U., Budil, D., and Freed, J. H., *Biophys. J.*, in press, 1991)].

Another potentially significant improvement would be to use a time-dependent gradient since this method gives the concentration profile in x-space directly. The method of recovering the concentration profile is conceptually similar to the sequential plane method in NMR imaging and was first used in EPR imaging by Herrling and coworkers.[59]

The use of pulsed-field gradients with the electron spin-echo (ESE) technique would be more promising. ESE-EPR imaging of the static concentration-profile with pulsed-field gradient was first executed by Milov et al.[60] The spin echo is observed after a ($\pi/2 - \tau - \pi - \tau$) sequence, and a pulse of the spatially uniform magnetic-field gradient is generated between either $\pi/2$ and π pulses or π pulse and the echo. Considering the amplitude of the spin echo after the ($\pi/2 - \tau - \pi - \tau$) sequence in the presence of the pulsed-field gradient, $A(\tau,q)$, and in the absence of the pulsed-field gradient $A(\tau,0)$, they showed that $A(\tau,k)/A(\tau,0)$ does not depend on τ, being only a function of k:

$$A(\tau,k)/A(\tau,0) \sim \int_{-\infty}^{\infty} C(x)e^{-2\pi ikx}dx \tag{37}$$

where $k = \gamma b_{J_x} q/2\pi$; γ is the magnetogyric ratio, $b_{J_x} = \dfrac{d^2B}{dJdx}$ is the gradient of the magnetic induction due to a unit current through the field-gradient coils, and q is the net electric charge which has flowed through the field-gradient coils during the pulse, i.e., $q = \int_0^{2\tau} J(t)s(t)dt$, $s(t) = 1$ for $t < \tau$ and $s(t) = -1$ for $t > \tau$, and J(t) is the current in field-gradient coils. Therefore, $A(\tau,k)/A(\tau,0)$ is the value of the Fourier-space concentration profile at k; $A(\tau,k)/A(\tau,0) = C(k)$. Thus, repeating the measurement of $A(\tau,q)$ over a wide range of q values, in principle, one should be able to recover the Fourier-space image of the concentration profile. On collecting the Fourier-space concentration profiles at different times t, one can then make use of the Fourier-space analysis described in Section IV in order to obtain the diffusion constant.

Fourier-transform (FT) EPR spectroscopy has recently become available.[55] Even though the principles of FT-EPR spectroscopy are identical to those of FT-NMR, it was a challenge to overcome the technical difficulties arising in the past from the shorter time scales, but the authors believe that in the near future it should be possible to extend of FT-EPR spectroscopy to FT-EPR imaging. [Added in proof: This has now been realized (Ewert, U., Crepeau, R. H., Lee, S., Xu, D., Dunham, C., and Freed, J. H., to be published). This also includes spectral-spatial ESR Imaging by FT methods utilizing short (ca. 100 nsec) pulsed field gradients as well as two-dimensional electron-electron double resonance as a function of spatial dimension, also by FT methods].

Now the authors wish to discuss a possible application of FT-EPR to the determination of the diffusion coefficient of spin probes in a solution (i.e., FT-DID) which would be comparable to the continuous wave (CW) EPR imaging of diffusion technique. Because of the speed of data collection (a single free induction decay or FID in a microsecond with successive averaging over a period of a millisecond), the errors originating from the finite sweep time in the CW-EPR method would be eliminated.

It is well-known that the FID in the time domain is a Fourier transform of the CW

spectrum in the frequency domain. For example, a simple exponential decay with transverse relaxation time T_2 in the time domain corresponds to a Lorentzian with width T_2^{-1} in the frequency domain and vice versa.[61] Suppose, for simplicity, that the spins in a sample yield a Lorentzian line of width T_2^{-1} resonant at an angular frequency ω_1. The spectrum also has an inhomogeneous broadening $h(\omega)$ due to the static local fields. Then, one will obtain a CW-EPR spectrum from this sample in the form of a convolution of the Lorentzian with $h(\omega)$:

$$S(\omega) = \int_{-\infty}^{\infty} h(\omega_a) \times \frac{T_2^{-1}}{[\omega - (\omega_a + \omega_1)]^2 + T_2^{-1}} d\omega_a \tag{38}$$

Upon Fourier transformation with respect to ω we obtain the FID signal after a $\pi/2$ pulse in the time domain τ:

$$s(\tau) = H(\tau)\, e^{-i\omega_1\tau} e^{-\tau/T_2} \tag{39}$$

where $H(\tau)$ is the Fourier transform of $h(\omega)$. Below, $H(\tau)$ shall have a characteristic decay constant T_2^* and $T_2^{*-1} \equiv T_2^{-1} + T_2^{\dagger -1}$.

Now, suppose that the sample has an inhomogeneous 1-D spin-probe distribution $C(x)$ and the static magnetic-field gradient (B') is applied along x. (In principle, pulsed-field gradients can be utilized for FT-EPR imaging as is the case of NMR imaging. In practice, however, it would not be trivial to achieve a pulsed-field gradient in 20 to 50 nsec.[62,63]) [Added in proof: It is now possible to achieve pulsed field gradients lasting ca. 100 nsec with B'_{max} 80 G/cm (cf. Ewert, U., Crepeau, R. H., Lee, S., Xu, D., Dunham, C., and Freed, J. H., to be published)]. Then, the resonant frequency ω_x of the spins at x would be $\omega_x = \omega_1 + \omega''$; ($\omega'' = \gamma B' x$). Thus, the resultant time domain signal would be:

$$s_{B'}(\tau) = \int_{-\infty}^{\infty} C(\omega'') H(\tau) e^{-i\omega_x\tau} e^{-\tau/T_2} d\omega'' \tag{40}$$

This can be written as:

$$s_{B'}(\tau) = H(\tau) e^{-i\omega_1\tau} e^{-\tau/T_2} \cdot \int_{-\infty}^{\infty} C(\omega'') e^{-i\omega''\tau} d\omega'' \tag{41}$$

It follows from Equation 41 that the FID signal in the presence of a field gradient is the product of the FID signal in the absence of the field gradient and the Fourier transform of the normalized concentration profile in the frequency domain:

$$s_{B'}(\tau) = s(\tau) \cdot C(\tau) \tag{42}$$

Since the concentration profile in Equation 42 is expressed in the time domain (τ-domain, an inverse of the frequency domain), for consistency with the notation used through this chapter, time-space must be converted to κ-space (which is an inverse of the ξ-domain). The angular frequency is related to ξ by $\omega = \gamma B = \gamma \xi B'$, so τ is related to κ by $\tau = 2\pi\kappa/(\gamma B')$.

Thus, the Fourier transformed (normalized) concentration profile can be obtained by dividing the gradient-on FID by the gradient-off FID:

$$C(\tau;t) = \frac{s_{B'}(\tau;t)}{s(\tau)} \tag{43}$$

or, equivalently,

$$C(\kappa,t) = \frac{s_{B'}(\kappa,t)}{s(\kappa)} \tag{44}$$

where $\kappa = (\tau\gamma B')/2\pi$. This analysis has been based on the assumption that the time-scales of relevance (i.e., $\tau < T_2, T_2^*$, see Equation 39) are short enough that the EPR signal is unaffected by the diffusion (i.e., $2DT_2^{*3}\gamma^2B'^2 \ll 1$), which is valid in EPR for $D < 10^{-1}$ cm^2s^{-1}.[31] This means that the time-scale of a single FID relates to a static concentration profile. A longer time ($t \gg \tau$) was introduced to measure the times over which significant diffusion occurs.

Once one collects Fourier-transformed concentration profiles at different times t, one can readily utilize the Fourier-space analysis method described in Section IV to obtain the diffusion coefficient. From Equation 44 one finds that the FIDs from a dynamic sample with diffusion coefficient D at two different times t_i and t_j are related by

$$\ln \frac{s_{B'}(\kappa,t_i)}{s_{B'}(\kappa,t_j)} = -4\pi^2k^2D\Delta t_{ij} \tag{45}$$

which is equivalent to Equation 24, see Section IV. Note that here, also, the gradient-off FID is cancelled out in the lhs of Equation 45 (see Equation 24).

The main advantage of the FT-DID method over CW-DID would be that the FID signal in the presence of a field gradient can be directly used to obtain D without any Fourier transform procedure. For static FT-EPR imaging, C(x) would be obtained directly from the Fourier transformation of Equation 44. One initial Fourier transform, however, is needed to obtain C(k) in CW-EPR imaging. Consequently, the possible numerical errors involved in the Fourier transform (which is inevitable in the CW-EPR method) can be reduced. Furthermore, since a single FID can be collected over a period of the order of a microsecond (with successive averaging requiring only a millisecond), it should be possible to greatly reduce the errors inherent in the finite sweep-times in the CW method, see Section III.

One of the main technical problems in performing this FID experiment is the inhomogeneous broadening of the EPR linewidth due partly to the static field gradient B'. Suppose the linewidth of the EPR spectrum in the presence of B' is 1 to 4 G. (For example, a typical linewidth for the ESR spectrum of a nitroxide spin-label in model membranes is 0.5 to 2 G. Assume the linewidth is doubled by the appropriate B'.) This inhomogeneous broadening corresponds to 66 to 15 nsec in the time domain. This would mean that most of the FID signal will decay away during the dead time, since at present the FID-EPR spectrometer has >50 nsec dead time after the microwave pulse. [Added in proof: At present, since B' can now be pulsed, it is applied only during the regular dead-time of the FID-EPR spectrometer, and the FID is detected only after B' is on (cf. Ewert, U., Crepeau, R. H., Lee, S., Xu, D., Dunham, C., and Freed, J. H., to published)]. A way of avoiding this problem is to collect the FID signal after an echo generated by $\pi/2 - \tau_1 - \pi$ pulse. Then, one can eliminate the dead time effect in the well-known fashion. That is, the complete FID signal is recovered from the echo according to

$$s_{B'}(2\tau_1 + \tau) = H(\tau)\exp(-i\omega_1\tau)\exp[-(\tau + 2\tau_1/T_2)] \cdot C(\tau) \tag{46}$$

However, a disadvantage of this technique is a decrease of the FID amplitude due to the homogeneous T_2. On comparing with Equation 41, the signal-to-noise ratio is reduced by a factor of $\exp(2\tau_1/T_2)$. Thus, for spin labels having short T_2, it would still be difficult to perform the FT-DID EPR experiment and would require extensive signal-averaging. However, it is the recommended time-domain approach when $T_2 \gg T_2^*$.

ACKNOWLEDGMENTS

J.K.M. acknowledges partial support of his visit to Cornell University by the Polish Academy of Sciences under Project CPBP 01.12. Dr. R. H. Crepeau is thanked for his comments during preparation of the manuscript. Supported by the National Institute of Health Grant Number GM-25862 and National Science Foundation Grant DMR-89-01718 and CHE 87-03014.

REFERENCES

1. **Luckhurst, G. R. and Gray, G. W.,** *The Molecular Physics of Liquid Crystals*, Academic Press, New York, 1978.
2. **Luckhurst, G. R. and Veracini, C. A.,** *The Molecular Dynamics of Liquid Crystals*, A NATO Advanced Study Institute, to be published.
3. **Anisimov, M. A.,** Critical phenomena in liquid crystals, *Mol. Cryst. Liq. Cryst.*, 162A, 1, 1988.
4. **Gennis, R. B.,** *Biomembranes: Molecular Structure and Function*, Springer-Verlag, New York, 1989.
5. **Svedberg, T.,** Electrical conduction in anisotropic liquids, *Ann. Phys. Leipzig*, 49, 437, 1916.
6. **Rondelez, F.,** Measurement of diffusion anisotropies in liquid crystals by use of dyes, *Solid State Commun.*, 14, 815, 1974.
7. **Hakemi, H. and Labes, M. M.,** Self-diffusion coefficients of a nematic liquid crystal via an optical method, *J. Chem. Phys.*, 63, 3708, 1975.
8. **Yun, C. K. and Fredrickson, A. G.,** Anisotropic mass diffusion in liquid crystals, *Mol. Cryst. Liq. Cryst.*, 12, 73, 1970.
9. **Rigaud, J. L., Gary-Bobo, C. M., Sanson, A., and Ptak, M.,** Fatty acids diffusion in lecithin multilayers: hydration and pH effects, *Chem. Phys. Lipids*, 18, 23, 1977.
10. **Heppke, G., Schneider, F., and Sterzl, A.,** Investigation of the electrical conductivity of homologous N-(4-n-alkoxybenzylidene)-4'-n-butylanilines in the nematic and smectic phases, *Z. Naturforsch.*, 31a, 1700, 1976 (in German).
11. **Krüger, G. J. and Spiesecke, H.,** Anisotropy of the diffusion coefficient in nematic liquid solutions measured by NMR techniques, *Z. Naturforsch.*, 28a, 964, 1973.
12. **Kuo, A.-L. and Wade, C. G.,** Lipid lateral diffusion by pulsed nuclear magentic resonance, *Biochemistry*, 18, 2300, 1979.
13. **Blinc, R., Burger, M., Luzar, M., Pirš, J., Zupančič, I., and Žumer, S.,** Anisotropy of self-diffusion in the smectic-A and smectic-C phases, *Phys. Rev. Lett.*, 33, 1192, 1974.
14. **Krüger, G. J.,** Diffusion in thermotropic liquid crystals, *Phys. Rep.*, 82, 229, 1982.
15. **Noack, F.,** NMR studies of self-diffusion in some homologous nematic liquid crystals, *Mol. Cryst. Liq. Cryst.*, 113, 247, 1984.
16. **Sheats, J. R. and McConnell, H. M.,** A photochemical technique for measuring lateral diffusion of spin-labeled phospholipids in membranes, *Proc. Natl. Acad. Sci. U. S. A.*, 75, 4661, 1978.
17. **Rubenstein, J. L. R., Smith, B. A., and McConnell, H. M.,** Lateral diffusion in binary mixtures of cholesterol and phosphatidylcholines, *Proc. Natl. Acad. Sci. U. S. A.*, 76, 15, 1979.
18. **Sheats, J. R.,** Lateral Diffusion in Phospholipid Membranes, Ph.D. thesis, Stanford University, Stanford, CA, 1978.
19. **Aha, M.,** Diffusion coefficients of paramagnetic species in solution, *J. Magn. Reson.*, 22, 289, 1976.
20. **Wang, J. H.,** Self-diffusion and structure of liquid water. I. Measurement of self-diffusion of liquid water with deuterium as tracer, *J. Am. Chem. Soc.*, 73, 510, 1951.
21. **Galtseva, E. U., Yakimchenko, O. Ye., and Lebedev, Ya. S.,** Diffusion of free radicals as studied by tomography, *Chem. Phys. Lett.*, 99, 301, 1983.
22. **Berliner, L. J. and Fujii, H.,** Magnetic resonance imaging of biological specimens by electron paramagnetic resonance of nitroxide spin labels, *Science*, 227, 517, 1985.
23. **Berliner, L. J. and Fujii, H.,** EPR imaging of diffusional processes in biologically relevant polymers, *J. Magn. Reson.*, 69, 68, 1986.
24. **Demsar, F., Cevc, P., and Schara, M.,** Diffusion of spin probes in tissues measured by field-gradient EPR, *J. Magn. Reson.*, 69, 258, 1986.
25. **Demsar, F., Swartz, H. M., and Schara, M.,** Use of field gradient EPR to measure diffusion of nitroxides in tissues, *Magn. Reson. Med. Biol.*, 1, 17, 1988.

26. **Demsar, F., Walczak, T., Morse, P. D., II, Bačić, G., Zolnai, Z., and Swartz, H. M.**, Detection of diffusion and distribution of oxygen by fast-scan EPR imaging, *J. Magn. Reson.*, 76, 224, 1988.
27. **Eaton, S. S. and Eaton, G. R.**, EPR imaging, *Spectroscopy*, 1, 32, 1986.
28. **Stemp, E. D. A., Eaton, G. R., Eaton, S. S., and Maltempo, M. M.**, Spectral-spatial electron paramagnetic resonance imaging and transport of radicals in nonuniform media, *J. Phys. Chem.*, 91, 6467, 1987.
29. **Maltempo, M. M., Eaton, S. S., and Eaton, G. R.**, Reconstruction of spectral-spatial two-dimensional EPR images from incomplete sets of projections without prior knowledge of the component spectra, *J. Magn. Reson.*, 77, 75, 1988.
30. **Hornak, J. P., Moscicki, J. K., and Freed, J. H.**, Translational diffusion coefficients by ESR imaging technique, presented at 7th Int. EPR Symp., Rocky Mountain Conference, Denver, 1984.
31. **Hornak, J. P., Moscicki, J. K., Schneider, D. J., and Freed, J. H.**, Diffusion coefficients in anisotropic fluids by ESR imaging of concentration profiles, *J. Chem. Phys.*, 84, 3387, 1986.
32. **Cleary, D. A., Shin, Y. K., Schneider, D. J., and Freed, J. H.**, Rapid determination of translational diffusion coefficients using ESR imaging, *J. Magn. Reson.*, 79, 474, 1988.
33. **Shin, Y. K., Cleary, D. A., Schneider, D. J., Moscicki, J. K., and Freed, J. H.**, Rapid determination of lateral diffusion coefficients in model membranes using ESR imaging, presented at the 8th Int. Conf. Magnetic Resonance in Biological Systems, Madison, Wisconsin, 1988.
34. **Shin, Y. K. and Freed, J. H.**, Dynamic imaging of lateral diffusion by electron spin resonance and study of rotational dynamics in model membranes: effect of cholesterol, *Biophys. J.*, 55, 537, 1989.
35. **Moscicki, J. K., Shin, Y. K., and Freed, J. H.**, Dynamic imaging of diffusion by ESR, *J. Magn. Reson.*, 84, 554, 1989.
36. **Moscicki, J. K., Shin, Y. K., and Freed, J. H.**, Dynamic imaging of diffusion in one dimension by cw-ESR, *Phys. Med.*, 5, 1989.
37. **Shin, Y. K., Moscicki, J. K., and Freed, J. H.**, Dynamics of phosphatidylcholine-cholesterol mixed model membranes in the liquid crystalline state, *Biophys. J.*, 58, 445, 1990.
38. **Eastman, M. P., Kooser, R. G., Das, M. R., and Freed, J. H.**, Studies of Heisenberg spin exchange in ESR spectra. I. Line width and saturation effects, *J. Chem. Phys.*, 51, 2690, 1969.
39. **Nayeem, A., Rananavare, S. B., Sastry, V. S. S. and Freed, J. H.**, Heisenberg spin exchange and molecular diffusion in liquid crystals, *J. Chem. Phys.*, 91, 6887, 1989.
40. **Wade, C. G.**, NMR relaxation in thermotropic liquid crystals, *Ann. Rev. Phys. Chem.*, 28, 47, 1977.
41. **Dianoux, A. J., Heidemann, A., Volino, F., and Hervet, H.**, Self-diffusion and undulation modes in a smectic-A liquid crystal: a high-resolution neutron-scattering study, *Mol. Phys.*, 32, 1521, 1976.
42. **Freed, J. H.**, Theory of slow tumbling ESR spectra for nitroxides, in *Spin Labeling, Theory and Applications*, Berliner, L. J., Ed., Academic Press, New York, 1976, 53.
43. **Schneider, D. J. and Freed, J. H.**, Calculating slow motional magnetic resonance spectra: a user's guide, in *Biological Magnetic Resonance*, Vol. 8, Berliner, L. J., Ed., Plenum Press, New York, 1989, 1.
44. **Crank, J.**, *The Mathematics of Diffusion*, Clarendon Press, Oxford, 1976.
45. **Morse, P. M. and Feshbach, H.**, *Methods of Theoretical Physics*, McGraw-Hill, New York, 1953.
46. **Bracewell, R. N.**, *The Fourier Transform and its Applications*, McGraw-Hill, New York, 1978.
47. **Press, W. H., Flannery, B. P., Teukolsky, S. A., and Vetterling, W. T.**, *Numerical Recipies: the Art of Scientific Computing*, Cambridge University Press, London, 1986.
48. **Rananavare, S. B., Pisipati, V. G. K. M., and Freed, J. H.**, ESR and DSC studies of n-alkyl m-alkoxybenzylidenes, *Liq. Cryst.*, 3, 957, 1988.
49. **Moscicki, J. K.**, Molecular dynamics in rigid-rod macromolecular lyotropic liquid crystals, *Adv. Chem. Phys.*, LXIII, 631, 1985.
50. **Moscicki, J. K., Robin-Lherbier, B., Canet, D., and Aharoni, S. M.**, DMR study of the magnetic field orientation of lyotropic nematic phase of poly(n-hexylisocyanate) solution in toluene-d_8, *J. Phys. Lett. (Paris)*, 45, L379, 1984.
51. **Fleischer, G. and Moscicki, J. K.**, Translational diffusion of poly(n-alkylisocyanate)s by NMR spin echo technique, to be published.
52. **Wee, E. L. and Miller, W. G.**, Studies on nitroxide spin-labeled poly-γ-benzyl-α,L-glutamate, *J. Phys. Chem.*, 77, 182, 1973.
53. **Doi, M. and Edwards, S. F.**, *The Theory of Polymer Dynamics*, Clarendon Press, New York, 1986.
54. **Altenberger, A. R. and Dahler, J. S.**, Kinetic theory of a concentrated suspension of axisymmetric solute particles, *Mol. Phys.*, 60, 1015, 1987.
55. **Gorcester, J. and Freed, J. H.**, Two-dimensional Fourier transform ESR correlation spectroscopy, *J. Chem. Phys.*, 88, 4678, 1988.
56. **Froncisz, W. and Hyde, J. S.**, The loop-gap resonator: a new microwave lumped circuit ESR sample structure, *J. Magn. Reson.*, 47, 515, 1982.
57. **Kochi, J. K.**, *Free Radicals*, John Wiley & Sons, New York, 1973.

58. **Sheats, J. R. and McConnell, H. M.**, Photochemical reaction of alkylpentacyanocobaltes with nitroxides: a new biophysical tool, *J. Am. Chem. Soc.*, 99, 7091, 1977.
59. **Herrling, T., Klimes, N., Karthe, W., Ewert, U., and Ebert, E.**, Zeugmatography with modulated magnetic field gradient, *J. Magn. Reson.*, 49, 203, 1982.
60. **Milov, A. D., Pusep, A. Yu., Dzuba, S. A., and Tsvetkov, Yu. D.**, Electron spin echo as a method of ESR tomography, *Chem. Phys. Lett.*, 119, 421, 1985.
61. **Abragam, A.**, *Principles of Nuclear Resonance*, Clarendon Press, Oxford, 1983.
62. **Hornak, J. P. and Freed, J. H.**, Eldor spin echoes and slow motions, *Chem. Phys. Lett.*, 101, 115, 1983.
63. **Maresch, G. G., Mehring, M., and Emid, S.**, High resolution ESR imaging, *Physica*, 138B, 261, 1986.

58. **Sheats, J. R. and McConnell, H. M.**, Photochemical reaction of alkylpentacyanocobaltates with nitroxides: a new biophysical tool, *J. Am. Chem. Soc.*, 99, 7091, 1977.
59. **Herrling, T., Klimes, N., Karthe, W., Ewert, U., and Ebert, E.**, Zeugmatography with modulated magnetic field gradient, *J. Magn. Reson.*, 49, 203, 1982.
60. **Milov, A. D., Pusep, A. Yu., Dzuba, S. A., and Tsvetkov, Yu. D.**, Electron spin echo as a method of ESR tomography, *Chem. Phys. Lett.*, 119, 421, 1985.
61. **Abragam, A.**, *Principles of Nuclear Resonance*, Clarendon Press, Oxford, 1983.
62. **Hornak, J. P. and Freed, J. H.**, Eldor spin echoes and slow motions, *Chem. Phys. Lett.*, 101, 115, 1983.
63. **Maresch, G. G., Mehring, M., and Emid, S.**, High resolution ESR imaging, *Physica*, 138B, 261, 1986.